Scaling of Impeller Response to Impeller-Diffuser Interactions in Centrifugal Compressors

by

David Landon Tarr

B.S., University of Colorado - Boulder (2006)

Submitted to the Department of Aeronautics and Astronautics
in partial fulfillment of the requirements for the degree of

Master of Science in Aeronautics and Astronautics

at the

MASSACHUSETTS INSTITUTE OF TECHNOLOGY

June 2008

Author .....
Department of Aeronautics and Astronautics
May 23, 2008

Certified by .....
Choon S. Tan
Senior Research Engineer, Gas Turbine Laboratory
Thesis Supervisor

Accepted by .....
David L. Darmofal
Associate Department Head
Chair, Committee on Graduate Students

Scaling of Impeller Response to Impeller-Diffuser Interactions in Centrifugal Compressors

by

David Landon Tarr

Submitted to the Department of Aeronautics and Astronautics
on May 23, 2008, in partial fulfillment of the
requirements for the degree of
Master of Science in Aeronautics and Astronautics

Abstract

A numerical investigation has been conducted to quantify the effect of impeller-diffuser interaction on changes in impeller performance. An assessment is made of the hypothesis that the nondimensional parameter characterizing impeller performance change due to interaction is the ratio of the radial gap between the impeller trailing edge and the diffuser leading edge to the diffuser vane pitch.

The time averaged results are found to show no measurable performance change with varying degrees of impeller-diffuser interaction, disproving the hypothesis. Analysis of the flow field shows that changes in loss and blockage due to interaction in the region of the blade leakage flow, which were expected to drive performance change, are negligible.

The disproven hypothesis lacks parameters to relate the level of impeller passage unsteadiness to the level of performance change due to interaction, which are shown to be important. The ratio of the unsteady amplitude, of blade leakage velocity or blade loading, to the time average value appears to be a parameter capable of quantifying the impact of unsteadiness on impeller performance change.

Thesis Supervisor: Choon S. Tan
Title: Senior Research Engineer, Gas Turbine Laboratory

Acknowledgments

I would like to express my gratitude to the people who have helped make this work possible. First and foremost I would like to thank my family, Lael, Emily and Steve, who have supported me throughout my endeavors, and especially during the difficult times. I could not have accomplished this without your constant support and confidence in my ability to succeed. Thank you.

I would like to thank my advisor, Dr. Choon Tan, for the opportunity to come study in the Gas Turbine Laboratory and to work on this interesting project.

My colleagues in the GTL played, perhaps, the largest role in the development of my education and enjoyment of my time here: Francois Le-Floch, for his boundless generosity and countless hours of help on anything from computer problems and P-sets, to learning the critical phrases of the French language. Barbara Botros, for her willingness to pass on her wisdom and advice, and for her social efforts which offered many great escapes from campus. Sean Nolin, for his help with TURBO, research advice abound, and the frequent work breaks in 31-257. Alfonso Villanueva for his mentoring sessions which jump-started my research experience. Ryan Tam for making office life easy, as well as his graphical expertise. And finally, all of the members of Aero-Astro intramural teams, whose victorious ways provided an outlet for the frustrations of research.

Thank you to all of the people who came to my assistance when difficulties were encountered: David Car, Professor Steve Gorrell, and Rick Roberts at the AFRL, Professor Jen-Ping Chen at the Ohio State University, Professor Robert Webster at the University of Tennessee - Chattanooga, Professor Edward Greitzer at MIT, and Dr. John Adamczyk at the NASA Glenn Research Center.

This work was supported by Army Research Office Award Number W911NF-05-1-0061, under ARO Scientific Officer Dr. Thomas L. Doligalski, and by the Navy Officer Scholarship Program, which allowed me to pursue this opportunity for a graduate education. This work was supported in part by a grant of computer time from the DoD High Performance Computing Modernization Program at the Air Force Research Laboratory Major Shared Resource Center. Thank you to the people and the programs of the DoD for their contributions to this work.

[0]The research reported in this document/presentation was performed in connection with the Army Research Office, under Award Number W911NF-05-1-0061. The views and conclusions contained in this document/presentation are those of the authors and should not be interpreted as presenting the official policies or position, either expressed or implied, of the U.S. Army or the U.S. government unless so designated by other authorized documents. Citation of manufacturers or trade names does not constitute an official endorsement or approval of the use thereof. The U.S. Government is authorized to reproduce and distribute reprints notwithstanding any copyright notation hereon.

Contents

Nomenclature

Latin Letters

A	Area	m^2	L^2
a	speed of sound	$\frac{m}{s}$	LT^{-1}
B	non-dimensional Blockage		
b	blade thickness	m	L
C_{PR_D}	Diffuser coefficient of pressure recovery		
CFD	Computational Fluid Dynamics		
¢	arbitrary constant		
D	diffuser		
G	I-D radial gap length	m	L
h	specific enthalpy	$\frac{J}{kg}$	$\mathrm{L}^2\mathrm{T}^{-}2$
i	quantity evaluated at an arbitrary meridional location		
I	impeller		
$\dot{m}$	mass flow rate	$\frac{kg}{s}$	MT^{-1}
M	Mach number		
$\hat{n}$	control surface unit normal		
N	blade count		
N_s	impeller rotational speed	rpm	T^{-1}
p	pressure	$\frac{N}{m^2}$	$\mathrm{ML}^{-1}\mathrm{T}^{-2}$
P.S.	pressure side		
Q	arbitrary quantity		

R	difference of specific heats	$\frac{J}{kg\,K}$	$L^2T^{-2}\Theta^{-1}$
r	radius	m	L
c_p	specific heat at constant pressure	$\frac{J}{kg\,K}$	$L^2T^{-2}\Theta^{-1}$
s	specific entropy	$\frac{J}{kg\,K}$	$L^2T^{-2}\Theta^{-1}$
S	vane/blade pitch	m	L
S.S.	suction side		
T	temperature	K	Θ
t	time	sec	T
v	absolute velocity	$\frac{m}{s}$	LT^{-1}
U	impeller speed, $r_{_{ITE}} \times \Omega$	$\frac{m}{s}$	LT^{-1}
W	specific work	$\frac{J}{kg}$	L^2T^{-2}
w	impeller-relative velocity	$\frac{m}{s}$	LT^{-1}

Greek Letters

α	absolute swirl angle (measured from meridional direction)	deg	
Λ	diffuser vane stagger angle (from radial)	deg	
β	reduced frequency		
Δ	change of a quantity		
δ	small increment operator		
η	adiabatic efficiency		
γ	ratio of specific heats		
θ	flow angle relative to meridional direction		
MFD	evaluated in the mean flow direction		
π	total-to-total pressure ratio		
ρ	density	$\frac{kg}{m^3}$	ML^3
σ	standard deviation		
VC	evaluated for the vaneless case		
Ω	impeller angular velocity	$\frac{rad}{s}$	T^{-1}

ω	vorticity	$\frac{1}{s}$	T^{-1}
ξ	loss potential	$\frac{J}{kg\,K}$	$L^2T^{-2}\Theta^{-1}$

Superscripts

$\hat{}$	unit vector
$'$	perturbation quantity
$\vec{}$	vector

Subscripts

<no subscript>	static quantity
corr	condition corrected quantity
E	quantity evaluated at edge of boundary layer
eff	effective quantity
∞	undisturbed free-stream value
i	quantity evaluated at an arbitrary meridional location
inj	quantity injected into domain
j	quantity evaluated at an arbitrary spanwise location
k	quantity evaluated at an arbitrary pitchwise location
VC	quantity evaluated for the vaneless case
ILE	evaluated at impeller leading edge
ITE	evaluated at impeller trailing edge
DLE	evaluated at diffuser leading edge
DTE	evaluated at diffuser trailing edge
BCG	evaluated at blade-casing gap

r	radial direction
ref	reference value
rel	quantity evaluated relative to rotating reference frame
$stage$	quantity evaluated over impeller, diffuser
SLE	evaluated at splitter leading edge
t	total (stagnation) quantity
tan	evaluated tangential to impeller velocity
VC	vaneless case
x	quantity evaluated in x-direction
y	quantity evaluated in y-direction
z	quantity evaluated in z-direction

List of Figures

List of Tables

Chapter 1

Introduction

1.1 Background and Motivation

Centrifugal compressors have historically not been researched as extensively as their axial counterpart due to the primary importance of axial compressors in military and commercial aircraft engines. They have been used in applications that require lower mass flow rates ($2.5 - 7\ kg/s$) and value low acquisition costs, simplicity and reduced weight over other parameters. Because of this, they have found their way into automotive engines as turbochargers, gas turbines for helicopters, auxiliary power units (APUs), and fuel pumps for rocket engines. Recently the advantages of centrifugal compressors have been exploited by the newly emerging light-business jet market as a highly efficient, weight-saving addition to the aft of an axial compressor [4], [5].

There are two key components to a centrifugal compressor: the impeller (rotor) and the diffuser (stator). The impeller pulls the working fluid in axially from the inlet as it rotates, turning the flow 90° away from the axis of rotation, and adding kinetic energy as the fluid accelerates radially outward. As the fluid exits the impeller with high velocity, it is the diffuser's role to then convert the kinetic energy into a static pressure rise by decelerating the flow before it leaves the compressor altogether. Since the channels of the impeller are rotating rapidly ($\sim 20,000$ rpm), a significant portion of the static pressure rise also comes from the centrifugal effect acting on the fluid. Similarly, the large radius change of the fluid increases the stagnation enthalpy

without necessarily increasing loss. This occurs because loss is dependent on the relative velocities in the impeller channel, which are not affected by a radius change in the impeller. With the combination of these two prominent qualities, it is not uncommon for single-stage pressure ratios to approach 8 : 1 whereas typical values for axial compressors are in the range of 1.4 : 1 [6].

Advances in computational abilities and CFD codes to capture flow details have improved significantly in recent years, allowing more detailed and comprehensive investigations to be conducted. Here, such advances are applied to better understand the fluid dynamic behavior governing impeller-diffuser interactions in centrifugal compressors with the goal of developing rational guidelines for design using the knowledge gained.

1.2 Previous Work

The two distinct components of the centrifugal compressor, the impeller and diffuser, combine to form the centrifugal compressor stage. Using models to estimate the performance of an isolated impeller or an isolated diffuser has been one approach taken to estimate the performance of a compressor. But because these two disparate components work together as a *system*, their performance together may not be the simple sum of their performances as considered in isolation. Viewing the compressor as a system begs the question: what effect do these components have on each other? The results of such an effect has been noticed by many investigators, yet no universal and rigorous guidelines for designing a compressor such that the two components are complimentary has been put forth with satisfactory results. Several researchers, including [7] have noted an optimum radial location of the diffuser leading edge, relative to the impeller, which produces a peak performance. Others have noted changes in the operating range when the number of diffuser vanes is varied. The exact mechanisms for these observations are not well understood. Summaries of other research efforts relating to the impeller-diffuser gap and its effect on performance can be found in either [6] or in [3].

The purpose of the current investigation is to continue working toward a universal description of performance effects due to interaction between the impeller and diffuser. Most recently, Shum [3] investigated impeller-diffuser interaction by varying the radial gap length. Under the conditions in which he conducted his experiment, he found that the major performance changes occurred in the impeller's efficiency and stagnation pressure rise and not in the diffuser, where the performance stayed relatively constant. This performance change in the impeller was attributed primarily to increased unsteadiness of the fluid leaking through the gap between the casing and the impeller blades. This 'blade leakage' flow in turn affected the entropy production and blockage in the impeller. Shum's assertion that the diffuser is relatively insensitive to mild distortions and changes in flow alignment is supported by the work of Phillips, [1]. Murray, [8], continued investigating interaction by varying the number of diffuser vanes, as well as the effect of blade-casing clearance on impeller performance. His results suggested that an optimum level of interaction did exist, and could be described by the parameters and one-dimensional model formulated by Shum, [3]. Murray put forth the hypothesis that the ratio of the impeller-diffuser gap length, G, to diffuser vane pitch, $S_{_D}$, is the parameter that characterizes the performance change due to varying degrees of impeller-diffuser interaction at a specified operating point [8]. The work here follows the work of both Shum and Murray closely, using the hypothesis of Murray and much of the analytical framework developed by Shum.

In 2003, Ziegler, et al. [9],[10], published a two-part physical experiment on impeller-diffuser interaction whose findings contrasted those of Shum and Murray. He found the impeller to be relatively insensitive to the diffuser and that the diffuser's performance drives the performance of the compressor system. His measurements also show that the change in performance between different radius ratios has a dependence on where on the π vs. $\dot{m}_{_{corr}}$ speed line the compressor is operating.

1.3 Goals of Present Work

Building upon the work of Shum, Murray and others, the overall objective of this research is to establish a set of scaling parameters that quantify the impact of impeller-diffuser interaction on centrifugal compressor performance. The specific technical objectives of this study are to:

1. Assess the hypothesis that changes in time averaged performance of an impeller due to impeller-diffuser interaction can be scaled by the ratio of impeller-diffuser gap to the diffuser vane pitch

2. Elucidate the behavior of the performance trend as related to the gap-to-pitch ratio, especially in the gap-to-pitch ratios near the hypothesized peak of performance (see figure 2-6).

3. Examine and quantify how specific flow mechanisms due to unsteady impeller-diffuser coupling influence overall performance as a function of the gap-to-pitch ratio

1.4 Thesis Scope and Content

To achieve these research objectives, a detailed interrogation of the computational flow field has been conducted. Chapter 2 describes the research compressor used in this study, the numerical solver and the computational approach taken. It also details how the experiment is designed in order to achieve the stated research objectives, as well as the performance metrics used to analyze the computational results. Chapter 3 presents the results of the computations on both a time average and unsteady basis. The nondimensional 'relative unsteadiness parameter' is introduced and used to explain the relatively low changes in loss observed in the blade leakage region. In Chapter 4, the results of the study are summarized and synthesized into a form that a future hypothesis might take to characterize impeller performance change due to impeller-diffuser interaction. It also uses the findings of the current work to suggest areas of continued research on this topic.

1.5 Research Contributions

- The hypothesis that the impeller performance change due to impeller-diffuser interaction can be described by a universal curve as a function of the gap to pitch ratio is disproven

- Additions to the hypothesis are needed in order to relate the level of impeller passage unsteadiness to the level of performance change due to interaction. For example, the ratio of the unsteady amplitude, of blade leakage velocity or blade loading, to the time average value appears to be a parameter capable of quantifying the impact of unsteadiness on impeller performance change

- Impeller unsteadiness level, as measured by the standard deviation of static pressures along the impeller passage centerline, is found to scale exponentially with the gap to pitch ratio only when the amplitude of the initial pressure perturbation produced by the diffuser remains constant

- A new method of quantifying relative changes in passage blockage is put forward. This method has the attributes of being easy to implement, is rigorously based, and is precise

Chapter 2

Technical Approach

2.1 Introduction

This chapter provides a description of the technical tools, the conceptual steps, and the physical reasoning used to achieve the research objectives defined in section 1.3. Because this study and many of the referenced studies use computational experiments to address the relevant technical issues, in this thesis they will be referred to generally as experiments. Any study that uses physical compressor rigs will be identified as such to avoid confusion.

2.2 Selection of Research Compressor

The $4:1$ pressure ratio NASA CC3 centrifugal compressor is the test article used in this study. Originally, the CC3 was designed as a high efficiency 1.66 $[kg/s]$ compressor by the Allison Engine Company and later scaled up to 4.54 $[kg/s]$ (10 $[lbm/s]$) to investigate the effect of scaling on efficiency [2]. The CC3 was selected for use in this study because it has been widely studied and offers a good amount of both numerical and physical data to which the baseline results of this study can be compared. Additionally, the nearly straight-channel wedge-type diffuser allows for relatively simple modification of the computational grid. Detailed geometric data on the CC3 can be found in [11]. The critical performance and geometric parameters are provided below:

- Corrected speed at design, $N_{s,corr} = 21,789$ $[RPM]$
- Impeller trailing edge radius, $r_{_{ITE}} = 21.57$ $[cm]$
- main blades = 15, splitter blades = 15, beginning at 30% impeller chord
- impeller blade backsweep angle, 50°
- local blade-casing clearance = 2% of the local blade span
- radius ratio of impeller exit to mean impeller inlet = 2.93
- radius ratio of diffuser channel exit to impeller exit = 2.09
- diffuser vanes, wedge shaped = 24
- diffuser vane stagger angle = 80.3°
- channel divergence angle = 7.92°
- impeller-diffuser gap length = 1.706 $[cm]$
- Gap to pitch ratio = 0.28

2.3 Computational Tools

2.3.1 Description of Flow-Solver

Analysis of the flow field is conducted using MSU TURBO, a three dimensional, unsteady, viscous, compressible CFD code developed at Mississippi State University. TURBO solves the Reynolds averaged Navier-Stokes equations in a rotating frame using an implicit, finite volume Newton-relaxation algorithm with modified Gauss-Seidel subiterations. Flow quantities are calculated with 2^{nd} and 3^{rd} order temporal and spatial accuracy, respectively. The turbulence model used is based on a decoupled two equation $\kappa - \epsilon$ scheme [12].

A strength of TURBO is its ability to capture time accurate relative motion between multiple adjacent blade rows rotating at different angular velocities. This is

done using a sliding interface across which the conservative variable quantities are interpolated to the appropriate grid elements on the opposing block. The single-passage representation of the compressor dictated by the use of phase lag boundary conditions (see section 2.3.3) does not allow flux-conserving local grid distortion techniques (LGD) to be implemented at sliding interfaces, thus necessitating the use of an equally accurate [13], but non-flux-conserving interpolation method.

The utility and accuracy of TURBO in relation to physical experiments will be discussed in section 2.4.

2.3.2 Computational Grid

TURBO utilizes structured, finite volume multi-block grids with arbitrary block connectivity. This allows users freedom to move, manipulate and examine complex portions of the grid without altering the grid continuity. The particular grid in this study uses 18 blocks to model the entire 2 blade row stage. Two blocks extend in parallel approximately one third of the impeller length upstream of the impeller inlet. Ten blocks are contained in the impeller, three in series for each blade passage (main blade and splitter blade) and four situated in the gap between the blade-tips and the casing (two per blade) to capture leakage related flow details. Blocks 13 and 14 span the vaneless space between the impeller and the diffuser, and blocks 15 through 18 connect the diffuser through the volute (figure 2-1). Each block is then assigned to be solved on one processor, in parallel with the others. The entire single-passage model consists of just under $900,000$ nodes.

The grid itself uses a Chebyshev polynomial node distribution across most passages to improve the flow resolution in critical regions where flow quantities are expected to have large gradients (e.g. near solid surfaces, corners, blade-casing gap regions). In regions that could not be modeled as channels, slightly different nodal spacings were used to capture the same critical flow elements. Figure 2-2 shows an example of such a distribution at the blunt trailing edge of the diffuser vanes. At the channel exit the distribution is concentrated near the vane corners with dense spacing relative to mid-channel, and in the wake of the vane a Chebyshev distribution

is used. This is because reverse flow associated with vane trailing edge separation is expected in this region and thus requires finer mesh to capture potentially important flow details.

2.3.3 Boundary Conditions

Phase-Lag Approximation

In order to conserve computational resources, a phase lag approximation is used so that only one blade passage per blade row needs to be modeled (one in the impeller, one in the diffuser). The use of phase lag boundary conditions enables compressors with spatially non-periodic ratios (greatest common factor is 1) of impeller blades to diffuser vanes to be modeled adequately using a single passage rather than modifying the geometry, using several passages, or using an entire annulus.

Solutions obtained from each time step of these single-passage simulations are stored by TURBO and used to update the passage boundary conditions in a temporally accurate manner based on the relative positions of the adjacent blades. In a full simulation this data would be obtained by simply passing the current data across the circumferential interface for each passage in the annulus. The result of using this approximation on a single passage grid is an immense savings in computational resources and thus an increase in the number of data points that can be analyzed with a given computer system. Barter and Chen,[13], showed that upwards of 70% savings in computation time can be attained by using the phase lag approximation with numerical results that are quantitatively similar to those of full simulations.

The underlying assumption of this method is that the effect of spatial periodicity on unsteadiness is of much lower order than that of temporal periodicity. Simulating a single passage means that the phase lag approximation will not capture any unsteadiness in the flow field caused by frequencies below that of the blade passing frequency. Such a condition may exist if there are large separated regions or vortex shedding at frequencies different than multiples of the blade passing frequency. This limitation of phase lag is not expected to be a problem for this study since the impeller blades

and diffuser vanes are smooth, and therefore not likely to cause massive flow separation in the region of the impeller trailing edge/diffuser leading edge, and because the simulation will be conducted at the operating point the CC3 was designed for.

Inlet Conditions

Conditions at the inlet of the computational domain are specified in the TURBO inputs using data taken from physical rig experiments of the CC3. Profiles of the stagnation temperature and stagnation pressure from the centerline of rotation to the outer radius of the impeller inlet are specified at eighteen points. During the simulation, these inlet stagnation profiles are held constant by TURBO. Plots of the profiles with radius can be seen in figure 2-3. The radial and tangential flow angles at the inlet are 18°.

To begin the simulation, an initial Mach number of $M = 0.15$ is specified throughout the domain. As the impeller angular velocity is increased to 100% of the design speed, the inlet Mach number is allowed to fluctuate to a new value.

Exit Conditions

At the exit of the computational domain, the static pressure is specified and adjusted to maintain the desired mass flow rate through the compressor. The boundary condition used corresponds to characteristic subsonic flow.

2.3.4 Post Processor

The solutions from TURBO are given in five nondimensional flow quantities indicated in table 2.1. From these five quantities, all pertinent flow variables can be computed. Several FORTRAN routines were modified for this task from a baseline code written largely by A.D. Villanueva [14] and B.B. Botros [15]. To obtain average performance values, additional scripts were written that can time average, mass average, area average, and mixed out average any flow quantity at any streamwise location over an arbitrary number of timesteps. Flow quantities that were not readily produced from

the five flow variables were extracted via a series of subroutines, several of which were the product of other generous researchers. Calculation of the dissipation function (equation 2.34) is done using a subroutine written by J. Adamczyk and B.B. Botros. Important grid dimensions, distances and areas were gathered with a routine from J. Adamczyk.

Since phase lag solutions presume that the flowfield is periodic with respect to the blade passing frequency, reconstruction of the full annulus flow field is possible by arranging the individual passage solutions in the correct manner. The post-processor used in this study has the ability to do this using the method outlined in [16]. Visualization of the post-processed data was done using routines written in MATLAB.

2.4 Code Validation

To determine the suitability of TURBO for use in this study, the overall performance parameters produced by TURBO for the as-designed geometry and using the phase lag approximation have been evaluated versus experimental data. The post processor described above is then compared to the performance parameters produced by the TURBO-generated performance file to ensure consistency. Figure 2-4 shows the speed lines taken at 80% and 100% corrected speed from TURBO and from the experimental rig test from [2]. The accuracy in both cases is within 5% of experiment for a given pressure ratio, but more importantly the trends are similar and consistent. Since this study is concerned with variations in performance with different levels of interaction, the precision of the relative trend is of greater significance than the absolute accuracy. As Smythe's data demonstrated, the corrected mass flows produced by TURBO are consistently several percentage points higher than rig values for a given back pressure [17]. Similarly, the phase lag results provided in [13] over estimate the mass flow by just over 1% while maintaining good accuracy relative to full annulus simulations. Referencing these other studies, the slightly higher mass flows seen in these results are typical of TURBO and therefore not of concern to the outcome of the experiment.

A thorough investigation of TURBO phase lag results versus physical experiment

is conducted in [18] for a compression system near stall. The study shows that the spatially accurate predictions of TURBO are well within the physical measurement uncertainties, indicating TURBO's suitability for use in compressor applications where detailed examination of the flow field is important to achieving the research goals.

The accuracy of the dissipation routine introduced in section 2.3.4 is a central concern here because the expected behavior is so dependent on localized mixing and entropy generation effects. The consistency of TURBO's results has been evaluated versus physical experiments both here and in other studies. Because of this, there is reasonable confidence in the entropy rise as calculated from TURBO's state-dependent variables. The dissipation routine is then tested by comparing the time averaged change in entropy through the compressor to the sum of the dissipation calculated over all elements in the computational grid. Because the dissipation routine calculates entropy generation at each cell, the accuracy of the integrated dissipation will give us insight into the accuracy of TURBO's flow solutions at the single-cell level. At the impeller exit, the mean discrepancy for all cases is less than 0.6%. The discrepancy between the integrated dissipation function and the entropy values calculated with state-variables are displayed in table 2.2. The quantities are calculated from the domain inlet to either the impeller exit or the diffuser exit.

The availability of this tool allows us to determine where entropy production, and therefore performance loss, is high within the compressor and how it changes with varying levels of interaction. Also, the agreement of the integrated dissipation with the state-calculated entropy suggests that the flow quantities of TURBO at the single-cell level are adequate for calculating changes in pertinent flow quantities. This assertion is especially true for the impeller, where the discrepancy is low and where we expect the important performance changes to occur.

2.5 Design of Computational Experiment

Accomplishing the stated research objectives relies on an experimental design that isolates the desired effect from other possible performance altering factors. To meet these objectives requires that a solid experimental foundation is laid that is both simple and analytically robust so that clear conclusions can be drawn. The second goal of this research, as laid out in section 1.3, is to substantiate and prove the hypothesis put forward by Murray, [8], for this specific compressor. The following sections detail the experimental design and highlight the physical reasoning that guides each decision.

2.5.1 Gap-to-Pitch Ratio

It was hypothesized by Murray, [8], that the gap to pitch ratio of a centrifugal compressor is the characteristic parameter governing the level of interaction between the impeller and diffuser. This can be understood by considering a simplified model in which the flow is considered to be irrotational. In this scenario it follows that each of the diffuser vanes produce a potential field whose influence would extend upstream. As this potential field reaches the impeller the pressure fields, and therefore the velocity fields, are altered, resulting in performance change. The extent to which the potential field nonuniformity influences upstream flow is dependent upon the characteristic spacing of the vanes, since Laplace's equation does not have an intrinsic length scale. Here, this spacing is identified as, S_D, the diffuser vane pitch. Greitzer, [19], solved the two dimensional equations of continuity and momentum for the upstream pressure perturbations of an infinite rectilinear cascade to find the solution in terms of a Fourier series,

$$p'(x,y) = p'(0,0) \sum_{k=-\infty, k\neq 0}^{\infty} e^{\left(\frac{2\pi|k|x}{S_D}\right)} e^{\left(\frac{2\pi iky}{S_D}\right)} \tag{2.1}$$

where the origin is taken to be at the blade leading edge, the y direction defined parallel to the row of blades, and x as the distance downstream of the blade leading

edge. The term $p'(0,0)$ indicates the initial pressure disturbance produced at the origin.

The use of this rectilinear cascade approximate a circular blade row (i.e. the vaned diffuser of a centrifugal compressor) is appropriate for ratios of the gap length to diffuser leading edge radius much less than unity. For the CC3 this ratio is: $G/r_{_{DLE}} = 0.07$. This value is small enough that the physical scaling of the problem should be captured by the rectilinear cascade model of Greitzer. [1]

The second exponential term on the right hand side of equation 2.1 reflects the spatial periodicity of the pressure perturbation along the blade row, and has no effect on the amplitude. Therefore, the scaling of the problem does not depend on this term and it will be considered a constant equal to one.

Since performance changes will be measured within the impeller it is most relevant to measure the strength of unsteadiness propagating upstream at the boundary of the impeller, that is, at the trailing edge. Substituting the location of the impeller trailing edge relative to the origin, $x = -G$, into equation 2.1, yields an expression for the amplitude of the unsteadiness at the impeller trailing edge:

$$p'(-G,0) = p'(0,0)e^{-\frac{2\pi G}{S_D}} \tag{2.2}$$

The characteristic ratio of the impeller-diffuser gap, G, to diffuser pitch, $S_{_D}$, appears here from this simple analysis. This result is the physical basis for the hypothesis put forth by Murray.

In deriving this equation no discussion of propagation rate is given. The disturbances felt upstream should depend on the decay rate with distance and time, which in turn should be related to the difference of the local speed of sound, a, and the flow velocity, v. In the rectilinear model, the important dimension for upstream influence is $-x$, but in a centrifugal compressor it is the relationship between these two velocities in the radial direction that is important when considering upstream influence.

[1] The corresponding solution for a centrifugal compressor would result in a modified Bessel function that would be expected to capture a similar exponential scaling between the gap and pitch length scales. For the purposes of the current investigation, the rectilinear approximation is deemed adequate.

As shown in Appendix A, the use of the acoustic approximation yields:

$$p'(-G,0) = p'(0,0)e^{-\frac{2\pi}{\left(\sqrt{1-M_r^2}\right)}\frac{G}{S_D}} \tag{2.3}$$

As the radial Mach number increases, pressure disturbances travel in the upstream-radial direction more slowly, allowing for greater disturbance decay prior to reaching the impeller. This effect can be interpreted as the radial Mach number in equation 2.3 stretching the gap length, G, effectively increasing the gap to pitch ratio, $G/S_{_D}$. Since this Mach related effect only retards the disturbance propagation in the direction opposite to the flow, the resulting pressure isobars should be skewed accordingly. Figure 2-5 shows the effect of this anisotropic propagation at the diffuser inlet of the CC3, $G/S_{_D} = 0.28$. This result shows that for different radial Mach numbers, which can occur due to changes in mass flow as well as from compressor to compressor, the exponential decay rate will be altered, causing a corresponding shift in the amplitude of the pressure perturbation felt at the impeller trailing edge.

Note that nothing has been said about the form of the coefficient $p'(0,0)$ in equation 2.2. The strength of this term is set largely by the blade shape and aerodynamic loading, which are controllable factors during design. Therefore, we assume that in seeking the optimum diffuser performance care is taken to adjust parameters so that the perturbation strength (incidence angle, $(\Lambda - \alpha)_{_{DLE}}$, and Mach number, $M_{_{DLE}}$, etc.) remains invariant. When comparing compressors with different diffuser designs, or at different operating points, it may be important to understand how the $p'(0,0)$ changes this influence. With this assumption, the propagation of the disturbance is then recognized as being of primary importance and not its magnitude. From an examination of equation 2.3 it is seen that this disturbance propagation is governed by the scaling ratio $\frac{G}{\left(\sqrt{1-M_{r,_{ITE}}^2}\right)S_{_D}}$.

In practice, the decay of the propagation will change since the radial Mach number varies as the flow diffuses out of the impeller. However, if the radial Mach number is consistently evaluated at the impeller trailing edge, $M_{r,_{ITE}}$, the exponent of equation 2.3 should provide a relative scaling between different flow rates and different com-

pressor designs and would serve as a useful initial indicator of impeller unsteadiness levels.

2.5.2 Selection of Gap-to-Pitch Ratios

To meet the goals stated in section 1.3, it is desired to match the time averaged performance by changing the gap length where previous studies altered the diffuser pitch. It is also a goal of this study to elucidate the performance trend as a function of $G/S_{_D}$ ratio. Doing this requires that data points be selected so as to isolate the effects associated with a change in $G/S_{_D}$ ratio as well as ensuring the feasibility of constructing an effective experiment to examine them. The data gathered by Shum [3] and Murray [8], seen in figure 2-6, suggests that there may be a peak in performance near $G/S_{_D} = 0.5$. In these plots, the vaneless case has arbitrarily been assigned a value of $G/S_{_D} = 1$. In order to substantiate the hypothesis that, as far as performance is concerned, changing the gap length is analogous to changing the diffuser pitch, a data point at $G/S_{_D} = 0.4$ is selected to which the result can be compared to Murray's data point for which he varied the diffuser pitch. To achieve the goal of more clearly defining the behavior of the trend in the peak region, $G/S_{_D} = 0.6$ is selected.

Impeller Tip Adjustment

The first attempt to modify the CC3 for this application was directed at lengthening or shortening the impeller blades in the radial direction, thereby changing the $G/S_{_D}$ ratio through the gap length, G. The effect of such a geometry change on performance was found using the Euler Turbine Equation, equation 2.4.

$$\Delta h_t = \Omega(r_{_{ITE}} v_{tan,_{ITE}} - r_{_{ILE}} v_{tan,_{ILE}}) \tag{2.4}$$

With the inlet conditions prescribed as in section 2.3.3 and the impeller exit quantities found using empirical relations and the impeller geometry, it was found that the work input would decrease by 8.00% to reach $G/S_{_D} = 0.4$. If the impeller was limited to a $\pm 1\%$ change in impeller radius, corresponding to a $\Delta G/S_{_D}$ of a mere 0.035, the

change in work would be $\sim$ 2.3%. Through Gibb's equation and the equation of state the change in stagnation enthalpy from Euler's equation can be related to the change in stagnation pressure. When this is done we find that, even when limiting the increase or reduction in the impeller tip radius to $\pm 1\%$, the stagnation pressure ratio from impeller inlet to exit will differ by $\sim 2.7\%$ from the current CC3 geometry. From the results of previous work seen in figure 2-6, it is clear that we are looking for changes in stagnation pressure on the order of $1 - 2\%$. If changes due to geometry alone account for a performance gain/reduction greater than that due to interaction, no conclusion would be able to be drawn. This analysis shows that the option of increasing or reducing the impeller tip is not a suitable approach for use in this investigation. Because the impeller is so sensitive to this small modification, this finding is suggestive that changes to the impeller are analogous to using an entirely different compressor. Any adjustment made to the impeller is likely to have such a large effect on the performance that the subtle changes important to most studies may be overshadowed. Therefore, for the selected objectives of this study, we assert that the impeller that defines the identity of a compressor and it is the impeller to which the diffuser must be designed to match. The key results of the tip-lengthening analysis are included in table 2.3.

Diffuser Vane Adjustment

Achieving the target $G/S_{_D}$ ratios must now be accomplished through modification of the diffuser and without varying vane-count as previous studies have done. This is accomplished by moving the individual vanes outward, but several complicating factors must be accounted for.

The first of these is the role of swirl angle, or equivalently the average diffuser vane incidence angle, on diffuser performance. Since the role of the diffuser is to convert the kinetic energy added by the impeller into a rise in static pressure, its key performance parameter is the coefficient of pressure recovery,

$$C_{PR_D} = \frac{p_{_{DTE}} - p_{_{DLE}}}{p_{t_{DLE}} - p_{_{DLE}}} \tag{2.5}$$

which is a ratio of the achieved static pressure rise to the ideal static pressure rise across the diffuser. This static pressure rise is obtained by a decrease in overall flow velocity. Component-wise, the radial velocity is reduced by an increase in radial flow area and the circumferential velocity is reduced by a torque applied by the diffuser vanes. The principal factor in determining this pressure rise is the ratio of flow areas between the channel inlet and exit, although compressibility effects play a role as evidenced by equation 2.11, below. In vaned diffusers this area ratio is determined exclusively by the swirl angle at the diffuser leading edge as shown in figure 2-7. For high swirl angles (measured from the radial), A_{DLE} is small, leading to large area ratios and large static pressure increases. In the CC3 the diffuser length is sufficient to align the flow with the channel at the diffuser exit and therefore the area, A_{DTE}, is unchanging with inlet swirl angle. To determine the dependence of the pressure ratio on the swirl angle and arrive at a one dimensional approximation, the flow is assumed to be a lossless (inviscid, adiabatic) ideal gas. Integrating equation 2.6 from the diffuser inlet (M_{DLE},A_{DLE}) to the diffuser exit (M_{DTE},A_{DTE}) yields equation 2.7.

$$\frac{dM^2}{M^2} = -2\frac{1+\frac{\gamma-1}{2}M^2}{1-M^2}\frac{dA}{A} \tag{2.6}$$

$$\ln\frac{A_{DTE}}{A_{DLE}} = \frac{1}{2}\left[\left(\frac{2}{\gamma-1}+1\right)\ln\left(1+\frac{\gamma-1}{2}M^2\right)-\ln M^2\right]_{M_{DLE}}^{M_{DTE}} \tag{2.7}$$

Knowing the stagnation pressure and Mach number, the static pressure can be found from the isentropic relation,

$$\frac{p_t}{p} = \left(1+\frac{\gamma-1}{2}M^2\right)^{\gamma/(\gamma-1)} \tag{2.8}$$

With geometric data from the CC3 and inlet Mach set to $M_{DLE} = 0.80$, the diffuser performance using this approximation is plotted in figure 2-8. The results indicate that the diffuser performance increases almost linearly with the swirl angle, and therefore the vane relative incidence angle, despite the area ratio having an exponential dependence on flow angle. This is confirmed experimentally in [20] and [21] and

computationally by [1]. From this it is clear that when the diffuser vanes are moved radially outward to alter the $G/S_{_D}$ ratio it is imperative that the angle of incidence angle on the vanes is maintained. Similarly, since the pressure disturbance created by the diffuser scales with the pressure loading across the diffuser vanes, an additional benefit of keeping the incidence angle the same from case to case is that the change in the term $p'(0,0)$ in equation 2.3 is minimized from case to case. Differences in this term will then be dominated by the differences in flow Mach number at the diffuser leading edge.

Changes in swirl angle with radius for a planar, isentropic, and uniform swirling flow, which occur in the vaneless space between the impeller and diffuser, can be quantified by examining equations 2.9 and 2.10 from Greitzer, et al [19].

$$\frac{dM^2}{M^2} = \frac{-2[1 + \frac{\gamma-1}{2}M^2]}{1 - M^2 cos^2\alpha}\frac{dr}{r} \tag{2.9}$$

$$d\alpha = \frac{[M^2 sin(2\alpha)]/2}{1 - M_r^2}\frac{dr}{r} \tag{2.10}$$

When these equations are used in combination, the swirl angle at any radius can be found for a known set of conditions at the impeller trailing edge. For the impeller exit conditions of the CC3 at 100% $N_{s,corr}$ the swirl angle is found at the radial locations corresponding to $G/S_{_D} = 0.4$ and $G/S_{_D} = 0.6$. Using this, the new vane stagger angle was set such that the predicted incidence angle matched that of the as-designed ($G/S_{_D} = 0.28$) configuration. The result of the restaggering process can be seen in table 2.4 and graphically in figure 2-9, which shows the projection of the channel as viewed from above the radial plane. The details of this method can be found in Appendix C.

As suggested earlier, the flow area through the compressor is of great importance in creating new diffuser geometries to target these gap-to-pitch ratios. Not only area ratio sets the overall static pressure recovery, but the streamwise flow area profile through the compressor determines the Mach number, local static pressure, flow velocity and boundary layer behavior. An expression can be found for the change of

static pressure with area by combining the momentum equation with the continuity equation for compressible flow,

$$\frac{dv}{v} = \frac{-dA/A}{1-M^2} \quad \text{with} \quad v\,dv = \frac{-dp}{\rho} \quad \text{yields} \Rightarrow \quad \frac{dp}{p} = \frac{dA}{A}\frac{\gamma M^2}{1-M^2} \tag{2.11}$$

The factor of $\gamma M^2/(1-M^2)$ due to compressibility means that as $M \rightarrow 1$, even small changes in area result in large changes in static pressure. Since the CC3 operates with transonic flow in the vaneless and semi-vaneless region, the streamwise area profiles must be tailored carefully to ensure that static pressure disturbances from case to case are due to the presence of vanes and not an unintended effect.

The restaggering of the vanes to account for variations in swirl angle was done by modifying only the footprint of the diffuser channel. Here, maintaining the streamwise flow area profile is accomplished by varying the depth of the channel along its length. The streamwise flow area profile of the as-designed diffuser ($G/S_{_D} = 0.28$) was calculated from the original grid at 79 locations, and then used as a template to create subsequent diffuser geometries. The appropriateness of this method was verified by comparison with the vaneless geometry used by Skoch,[2], in his physical rig study. Figure 2-10 shows the comparison of channel depth profiles for the vaneless case. Since the footprints are identical, the similarity of the depth profiles means the flow areas are also similar. The slight difference between the two profiles at the radial location of 11 $[in]$ is from the choice to approximate the experimental hub as being linear with radius.

By designing the new diffuser geometries in the manner described above, any performance change would be independent of flow area variations, altered flow angles, or increased vane loading.

2.5.3 Selection of Test Condition

The experimental results presented by Ziegler, et al. [9] [10], suggest that the effect of varying the radial gap on overall performance may depend on where the test-point lies

on the π_{stage} vs. $\dot{m}_{corr}$ speed line (seen in figure 2-4). For this reason it is important that we specify what values of corrected mass flow are to be examined and provide justification for their selection. This study is primarily concerned with operation near the design point, which is traditionally set through compromise of customer requirements for π and $\dot{m}_{corr}$, the machine's point of optimum η_{stage} and determination of the required stall margin. This compromise is driven in large part by cost and offers no quantifiable definition that can be applied consistently to compressors of all types. Therefore, to be technically consistent and maintain the generality of our results, we seek a new definition of the design point. In section 2.5.2 it was suggested that the impeller defines the identity of the compressor and that a complementary diffuser must be constructed to realize further improvements in performance. Therefore the potential of any impeller can be assessed most effectively with the case of zero interaction using a vaneless diffuser.

A second constraint is required to specify the mass flow rate at the point of operation: either the stagnation pressure ratio, or the efficiency. Denton, [22], offers the opinion that:

> *"Efficiency is probably the most important performance parameter for most turbomachines... [because] a small change in the efficiency of either component [compressor or turbine] causes a much larger proportional change in the power output."*

Also, the pressure ratio often continues to increase right up to compressor stall, meaning that no clear maximum or optimum point exists to which all cases can be converged and stabilized in a numerical simulation. For that reason the stagnation pressure ratio is not meaningful to employ as a constraint in this investigation. Following this logic, the design point is chosen to be the corrected mass flow rate where the maximum efficiency, η_{stage}, is obtained for a given impeller when it is coupled with a vaneless diffuser at 100% corrected speed. [1]

[1] Here the definition of corrected speed, $N_{s,corr}$, is assumed to be a given value that is set primarily by turbine design limitations due to its high loading and thermal stresses.

The rig data presented by Skoch et al, [2], shows a peak efficiency plateau occurring between $\dot{m}_{corr} = 4.56 - 4.74\frac{kg}{s}$. This data was then used to target the likely point of peak efficiency in the TURBO simulation of the vaneless case. The results from TURBO also show a plateau in the peak efficiency, seen in figure 2-11, therefore a median value of $\dot{m}_{corr} = 4.668\frac{kg}{s}$ was selected as the mass flow corresponding to a peak efficiency value.

2.5.4 Convergence

The criteria for convergence of simulations using the phase-lag approximation is outlined in [16]. In this study the back pressure is adjusted in an iterative process to reach the corrected mass flow specified in section 2.5.3. Of equal importance in establishing the test condition is determining the acceptable tolerance of corrected mass flow to which all test cases must be converged on a time averaged basis. If too high a tolerance is allowed, then perceived performance changes may be a result of changing the operating point on the π_{stage} vs. $\dot{m}_{corr}$ or η_{stage} vs. $\dot{m}_{corr}$ speed line and not due to interaction related effects. Previous studies, including [8], have found $\pm 1\%$ of the target mass flow to be an acceptable value for unknown reasons. Shum, [3], selected this value, but verified post priori that the performance changes were not simply due to mass flow variations.

The current hypothesis is predicated on detecting a change in stage stagnation pressure ratio, $\pi_{t,I}$, and stage efficiency, η_I as interaction level with the diffuser varies. The chosen tolerance in corrected mass flow should produce changes in these quantities several times smaller than the expected changes due to interaction in order to properly resolve the changes due to interaction alone. The pressure and efficiency data from the $G/S_{_D} = 0.28$ speed line (see figure 2-4) was used in conjunction with a Laplacian interpolation polynomial to determine the tolerance at the target operating point before the numerical experiment. Although this data is for the entire stage, it is the best available option to determine the sensitivity a priori. As long as diffuser performance remains similar from across the $G/S_{_D}$ ratios tested, this approximation will be adequate. Numerical results from previous experiments (figure 2-6) suggest

we expect changes in $\pi_{t,I}$ of $\sim 2\%$. To capture changes of this magnitude we set our allowable range of $\pi_{t,I}$ to less than 0.6% of the pressure ratio, resulting in a corrected mass flow tolerance of $\pm 0.01 \frac{kg}{s}$.

Due to the periodic nature of the mass flow with time, it is possible for this time averaged value to be within the tolerance yet have the peak amplitude lie well outside the tolerance window. To prevent this, an additional criterion is included that requires the standard deviation of each vaned case to be less than that of the vaneless case. Convergence of the vaneless case itself is considered to be achieved when the time averaged performance is invariant over the previous one, three, and five impeller revolutions. With all of these considerations, the new technical definition laid out above specifies the design point to be:

$$\overline{\dot{m}}^{\mathbf{t}}_{corr,design} \;=\; 4.668 \pm 0.01 \,\frac{kg}{s} \quad \text{and} \quad N_{s,corr} = 21789\, rpm \quad (\Omega = 363.15\, rad/s) \tag{2.12}$$

By comparison, a $\pm 1\%$ tolerance in the corrected mass flow could result in a pressure ratio variation of $\pm 3.5\%$, too large to isolate the effect of interaction. The results of studies conducted using the CC3 with tolerances of this magnitude are therefore interpreted with caution.

Speed lines from Ziegler's data, [9], and the CC3 specific data from Skoch, [2], show a general flattening trend as increasing gap distance, G, opens the diffuser throat and raises the mass flow at which choking occurs. This means that the tolerance found for $G/S_{_D} = 0.28$ represents the smallest required tolerance for the cases being examined and satisfies the tolerances for all larger gap to pitch ratios.

The precision and accuracy at which the results were obtained relative to the design point are displayed in table 2.5.

2.6 Performance Metrics

This section outlines the methods used to evaluate and quantify performance changes between the four geometric configurations.

2.6.1 Averaging Methods

To characterize the flow across an arbitrary plane or region by a single scalar or vector quantity, some information about the flow is necessarily lost. The manner in which this reduction of information is carried out is dependent on the eventual use of the data, and so the end-use of the data must be considered prior to selecting an appropriate averaging method and interpreting the results. The methods highlighted here represent the methods used in the analysis to follow.

Area Averaging

Area averaged quantities are defined as:

$$\overline{Q}^{\mathbf{A}} = \frac{\int_A Q dA}{\int_A dA} \tag{2.13}$$

where the subscript, A, on the integral represents an integration over an arbitrary surface. Area averaging a quantity is typically used when considering static pressures acting on a surface, since the area integral of the pressure experienced at every point is the net force on that surface. It should be noted that area averaging weights the quantity, Q, the same at every area element, dA.

Mass-flux Averaging

When average quantities of extensive properties are desired over a surface, A, it is necessary to weight the property by the amount of mass flowing through the region, dA. The 'weighting' of the mass-flux averaging method represents the extensive properties of the flow in a more accurate manner than simple area averaging. Mass-flux averaging an arbitrary quantity, Q is defined as:

$$\overline{Q}^{\mathbf{M}} = \frac{\int_A Q \, d\dot{m}}{\int_A d\dot{m}} \tag{2.14}$$

Flux dependent quantities such as entropy, velocity, stagnation pressure and stagnation temperature are mass averaged when their average value is desired. Intensive

quantities (generally static quantities) are not mass-flux averaged because, as Cumpsty points out, *"a mass average of static pressure is not a meaningful quantity"* [23].

Momentum-flux Averaging

Occassionally it is desired to find quantities based on the average momentum-flux of the flow. When this is the case, the momentum-flux average of a quantity is used. It is defined as:

$$\overline{Q}^{\mathbf{P}} = \frac{\int_A Qv\, d\dot{m}}{\int_A v\, d\dot{m}} \tag{2.15}$$

When considering parameters that are driven by velocity as well as mass flux, momentum-flux averaging is the appropriate method to use. Typically such parameters involve a need to assign an average direction to a flow field or to target momentum-related quantities such as fluid impulse. For the blockage calculations of section 2.6.2, the mean flow direction is defined using momentum averaging.

Mixed Out Averaging

Mixed out quantities are defined as those quantities that would exist if a given flow field were allowed to mix freely, until all nonuniformities had been removed and the pertinent flow variables could be characterized by a constant value across the channel. Calculating these uniform values is most often conducted while holding the flow area constant, as it is done here, but can also be conducted while holding the static pressure constant. The mixed out averaging procedure used here solves the following equations to yield the relevant quantities in a three dimensional, compressible, and rotating reference frame.

$$\int_A \rho w \left(\hat{w} \cdot \hat{n}\right) dA \;=\; \overline{\rho}^{\mathbf{X}} \overline{A}^{\mathbf{X}} \left(\overline{\hat{w}}^{\mathbf{X}} \cdot \hat{n}\right) \;=\; \dot{m} \tag{2.16}$$

$$\int_{A_x} p dA_x \;+\; \int_A \rho w \left(\hat{w} \cdot \hat{n}\right) w_x\, dA \;=\; \overline{p}^{\mathbf{X}} \overline{A}_x^{\mathbf{X}} \;+\; \dot{m} \overline{w}_x^{\mathbf{X}} \tag{2.17}$$

$$\int_{A_y} p dA_y \; + \; \int_A \rho w \left(\hat{w} \cdot \hat{n}\right) w_y \, dA \; = \; \overline{p}^{\mathbf{X}} \overline{A}_y^{\mathbf{X}} \; + \; \dot{m} \overline{w}_y^{\mathbf{X}} \tag{2.18}$$

$$\int_{A_z} p dA_z \; + \; \int_A \rho w \left(\hat{w} \cdot \hat{n}\right) w_z \, dA \; = \; \overline{p}^{\mathbf{X}} \overline{A}_z^{\mathbf{X}} \; + \; \dot{m} \overline{w}_z^{\mathbf{X}} \tag{2.19}$$

$$\frac{1}{\dot{m}} \int_A \rho w \left(\hat{w} \cdot \hat{n}\right) T_t \, dA \; = \; \overline{T}^{\mathbf{X}} \; + \; \frac{1}{2\, c_p} \left[\left(\overline{w}_x^{\mathbf{X}}\right)^2 \; + \; \left(\overline{w}_y^{\mathbf{X}} - \Omega \overline{z}\right)^2 \; + \; \left(\overline{w}_z^{\mathbf{X}} + \Omega \overline{y}\right)^2 \right] \tag{2.20}$$

$$p = \rho R T \tag{2.21}$$

This last equation is the perfect gas equation of state, and is used to remove the static temperature variable from equation 2.20. When the integrals on the left hand side of these equations are found from the numerical results, they can be solved to yield a quadratic for each of the components of relative velocity, $\vec{w} = [w_x \; w_y \; w_z]$. One set of solutions is not physical, and therefore cannot be correct. The other allows the rest of the mixed out conditions to be found. Although mixing rarely occurs to completion, the mixed out properties provide an upper bound from which the effects of mixing on the flow variables in question can be understood.

Time Averaging

For cases where it is desired to examine the general trends of the flow field over a period of time, the unsteady solutions are averaged with:

$$\overline{Q}^{\mathbf{t}} = \frac{\sum_{i=1}^{m} Q}{m} \tag{2.22}$$

Where m represents the number of time steps over which the quantity is to be averaged. In general, m is defined such that an integer number of blade passing periods is covered and such that each time step within that passing period is averaged with equal weight. A summation sign is used to highlight the discrete nature of the solu-

tion files.

When flow quantities are time averaged, the process is represented with the integral:

$$\overline{Q}^{\mathbf{t}} = \frac{\int_0^t Q\, dt}{t} \tag{2.23}$$

Time averaging is commutative with the other physical parameter based averaging methods.

2.6.2 Loss, Blockage and Slip

Shum's analysis of performance variations due to unsteady impeller-diffuser interaction focused on changes within the impeller only, as he found the changes there to be seven times more significant than those in the diffuser [3]. The parameters that he identified as major contributors to changes in impeller performance are:

- Loss
- Blockage
- Slip

He found that as the radius ratio of the diffuser leading edge to the impeller trailing edge decreased, the amount of slip and blockage were reduced, while loss generation increased. His results suggest that an optimum placement exists where the balance of these competing effects yield a peak in performance. To explain these changes, a modified version of the Euler Turbine Equation, 2.24, was linearized with respect to the independent variables, s and $v_{\tan}$. The result is equation 2.25 for changes in stagnation pressure and equation 2.26 for changes in static pressure.

$$\frac{p_{t,ITE}}{p_{t,ILE}} = \left[1 + \frac{v_{tan,ITE}(r_{ITE} \times \Omega)}{c_p T_{t,ILE}}\right]^{\gamma/(\gamma-1)} \exp\left(-(s_{ITE} - s_{ILE})/R\right) \tag{2.24}$$

$$\frac{\Delta p_{t_{ITE}}}{p_{t_{ITE}}} = ¢_A \left(\frac{\Delta A_{eff}}{A_{eff}}\right) + ¢_s \left(\frac{\Delta s_{ITE}}{c_p}\right) + ¢_\alpha \left(-\Delta\alpha\right) \tag{2.25}$$

$$\frac{\Delta p_{ITE}}{p_{ITE}} = ¢_{\tilde{A}} \left(\frac{\Delta A_{eff}}{A_{eff}}\right) + ¢_{\tilde{s}} \left(\frac{\Delta s_{ITE}}{c_p}\right) \tag{2.26}$$

The coefficients ¢$_A$ and ¢$_{\tilde{A}}$, ¢$_s$ and ¢$_{\tilde{s}}$, and ¢$_\alpha$ represent the coefficients of effective area (blockage), entropy generation (loss), and swirl angle (slip), respectively. In the following subsections the coefficients of the linearized model and their physical insights will be discussed as they pertain to the investigation at hand.

Slip

Ideally, the flow angle at the impeller trailing edge would match the blade angle. In reality there is a discrepancy between these two angles due to the effects of being in a rotating reference frame. As the flow nears the impeller exit, the pressures across the channel begin to equalize such that the pitchwise pressure gradient at the impeller trailing edge is significantly less than higher in the passage (similar to the Kutta Condition). As the pressure gradient from the pressure surface to suction surface decreases, the effect of the Coriolis force ($2\,w \times \Omega$) tends the flow in the direction opposite that of rotation. Because this phenomenon is an effect of the passage rotation, inviscid models, such as that in Greitzer, et al [19], are able to well describe the behavior. Referring to the Euler turbine equation, equation 2.4, it can be seen that an increase in the impeller relative flow angle due to slip means a decrease in the circumferential velocity and a decrease in the associated work input of the compressor. Since we have chosen to restrict geometric modification to the diffuser, any change in the slip must be due to the presence of the diffuser vanes downstream of the impeller. Shum's linearized model defined the slip influence coefficient to be:

$$¢_\alpha = \left(\frac{1}{\tan\alpha}\right)\left(\frac{\gamma}{\gamma-1}\right)\left(\frac{v_{tan,ITE}(r_{ITE}\times\Omega)}{c_pT_{t,ILE}+v_{tan,ITE}(r_{ITE}\times\Omega)}\right)\,0 \tag{2.27}$$

Since $0° \leq \alpha \leq 90°$, and $v_{tan,ITE}(r_{ITE}\times\Omega) > 0$, ¢$_\alpha$ will be greater than zero. Therefore, slip should be reduced as much as possible to maximize the stagnation pressure rise.

Blockage

Flow area reduction in internal flows means increased core velocity and a corresponding decrease in pressure rise capability. Khalid, [24], showed that performance changes

cannot be explained by losses and average flow speed alone, and that effective flow area reduction must be accounted for. To do this we must find an expression for the term ΔA_{eff} in equations 2.25 and 2.26, where blockage and effective area are related by:

$$1 - B = \frac{A_{eff}}{A_{geometric}} \tag{2.28}$$

From the definition of blockage, as expressed in [24], only the component of the velocity in the mean flow direction contributes to the value of B. In two dimensions the integral relation for blockage is the displacement thickness: the difference in flow area needed to pass the same mass flow when comparing inviscid and viscous flows. For compressible flows this is defined as:

$$\delta^* = \int_0^{y_E} \left(1 - \frac{\rho\, v_x}{\rho_E\, v_E}\right) dy \tag{2.29}$$

where the subscript $'E'$ denotes quantities evaluated at the edge of the boundary layer (beginning of core flow region), δ and x is in the direction of the free-stream.

The methods that others have developed for blockage quantification in three-dimensions are deemed either too cumbersome or too arbitrarily defined for application to centrifugal compressors. Therefore an alternative method for quantifying relative changes in blockage is offered which is shown to be similar to, and more rigorous and precise than Murray's method. The derivation and evaluation of this method can be found in Appendix B. The resulting expression is:

$$\frac{\Delta A_{eff}}{A_{actual}} = \frac{\dot{m}}{A_{actual}} \left(\frac{\overline{\rho\, w}^{\mathbf{t},\Upsilon}\big|_{caseX} - \overline{\rho\, w}^{\mathbf{t},\Upsilon}\big|_{ref}}{\overline{\rho\, w}^{\mathbf{t},\Upsilon}\big|_{caseX} \overline{\rho\, w}^{\mathbf{t},\Upsilon}\big|_{ref}} \right) \tag{2.30}$$

where the quantities $\overline{\rho\, w}^{\Upsilon}$ are the products of ρ and w in the core region of the passage. These 'core quantities' are calculated across a passage by time and momentum averaging the quantity $\rho\, \vec{w}$. The momentum average is weighted by the terms with the gradient and Laplacian of velocity in order to capture the value of $\rho\, \vec{w}$ in the core

region more accurately. In explicit form, this averaging method is:

$$\overline{\rho\, w}^{\Upsilon}_{core} = \frac{\int_A \rho\, \vec{w}^2_{MFD} \left(1 - \frac{|\nabla \vec{w}|}{|\nabla \vec{w}|_{max}}\right)\left(1 - \frac{|\nabla^2 \vec{w}|}{|\nabla^2 \vec{w}|_{max}}\right) d\dot{m}}{\int_A \vec{w}_{MFD} \left(1 - \frac{|\nabla \vec{w}|}{|\nabla \vec{w}|_{max}}\right)\left(1 - \frac{|\nabla^2 \vec{w}|}{|\nabla^2 \vec{w}|_{max}}\right) d\dot{m}} \tag{2.31}$$

Using this to find an appropriate estimation of $(\rho\, w)|_{core}$, equation 2.30 can then be used directly to find the associated quantity needed for Shum's one-dimensional performance model. The blockage coefficients, as defined by Shum, are:

$$¢_A = \left[\frac{\gamma\left((r_{ITE} \times \Omega) - v_{tan,ITE}\right)}{(\gamma - 1) v_{tan,ITE}}\right]\left(\frac{1}{1 - M^2_{rel,ITE}}\right)\left(\frac{v_{tan,ITE}(r_{ITE} \times \Omega)}{c_p T_{t,ILE} + v_{tan,ITE}(r_{ITE} \times \Omega)}\right) \tag{2.32}$$

$$¢_{\tilde{A}} = \frac{-\gamma M^2_{rel,ITE}}{1 - M^2_{rel,ITE}} > 0 \tag{2.33}$$

Loss

A measure of the lost work is determined by the product of entropy generated from irreversible processes with an appropriately selected temperature. Throughout the compressor, regions of high entropy production indicate the location and intensity of lost work, and therefore efficiency reduction. For adiabatic flow, the rate of entropy generation per unit volume can be found from:

$$\rho \frac{Ds}{Dt} = \frac{1}{T}\tau_{ij}\frac{\partial u_i}{\partial x_j} + \frac{k}{T^2}\left(\frac{\partial T}{\partial x_i}\right)^2 \tag{2.34}$$

where τ_{ij} is the stress tensor, k is the thermal conductivity, and x_i is the spatial coordinate vector. This equation for the rate of entropy generation is commonly known as the dissipation function, and will be referred to as such.

From inspection of the terms of equation 2.34, it can be seen that entropy is generated from gradients in static temperature and velocity. Flow through the small gap between the blade tip and the casing is one such region of high entropy production in centrifugal compressors. This blade leakage flow acts as a jet entering the impeller channel, producing large shear leading to high viscous losses. As Murray's research

suggests, increased levels of interaction have a pronounced effect on the strength of the blade leakage flow, and thus on the entropy produced. The numerical integration of equation 2.34 will allow us to compare the regions of entropy generation and identify the processes that are leading to improved or reduced performance. It is possible for the location of entropy production to be well downstream of where the velocity nonuniformity was introduced, making identification of the origins of performance loss difficult. This *potential* for loss does not appear in the dissipation function until it mixes out downstream. The use of mixed out averaging allows us to evaluate where the nonuniformity that potentially leads to loss is introduced and determine the maximum effect of such sources. The loss coefficients for the linearized one-dimensional performance prediction model are:

$$¢_s = -\left(1 + ¢_A\right)\left(\frac{\gamma}{\gamma - 1}\right) < 0 \tag{2.35}$$

$$¢_{\tilde{s}} = -\left(1 + ¢_{\tilde{A}}\right)\left(\frac{\gamma}{\gamma - 1}\right) < 0 \tag{2.36}$$

2.7 Summary

The technical framework that is used to achieve the goals stated in section 1.3 has been presented in this chapter. The background and important characteristics of the research compressor that has been selected for use were explained as well as the definition and justification of the operating point used. The numerical solver MSU TURBO used to model the CC3 compressor was described in section 2.3.1. The phase-lag approximation it uses to reduce computational resources has been explained, and the results of using TURBO to model the CC3 with this approximation have been validated.

Section 2.5 details how the computational experiment was designed. The selection process of the four gap to pitch ratios, including the vaneless case (which serves as the control case and the case by which performance changes were normalized), was delineated as well as the methods by which the geometric modifications were made.

The second half of this chapter has been an overview of the performance metrics that will be used to analyze the flow data after it has been deemed converged by the criteria of section 2.5.4. This overview has covered the methods used to average pertinent flow quantities as well as the metrics of loss blockage and slip, and how they are accounted for in Shum's linearized model for impeller performance change.

The following chapters use the numerical results obtained using the approach that has been outlined here to achieve the goals stated in section 1.3.

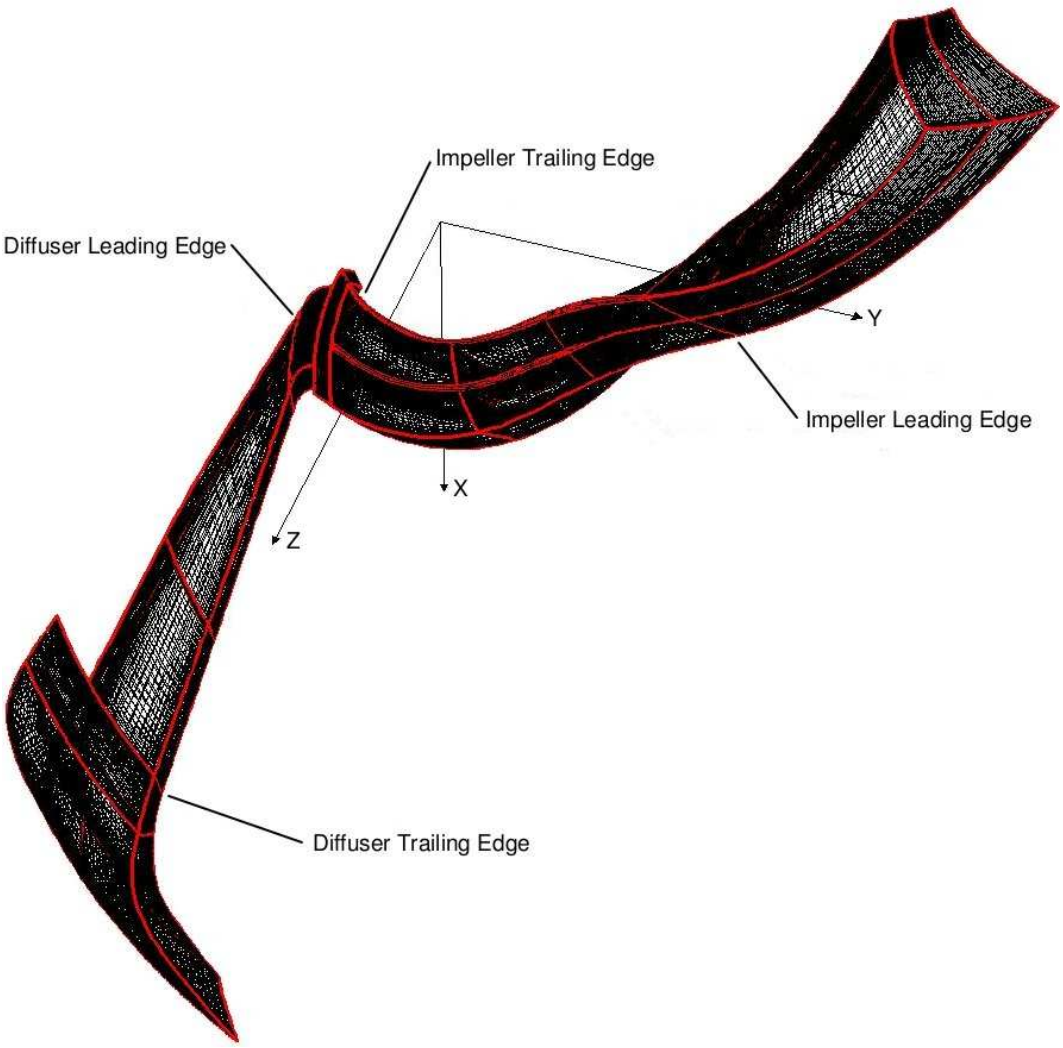

Figure 2-1: Single passage computational domain, $G/S_D = 0.28$ arrangement shown

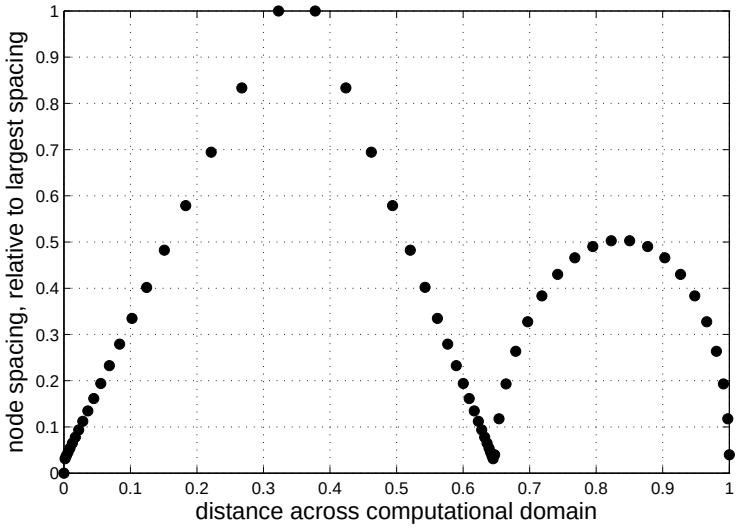

Figure 2-2: Example of node distribution profile at the diffuser trailing edge. Channel exit resides between values of 0 and 0.65 . The vane trailing edge distribution extends from 0.65 to 1.

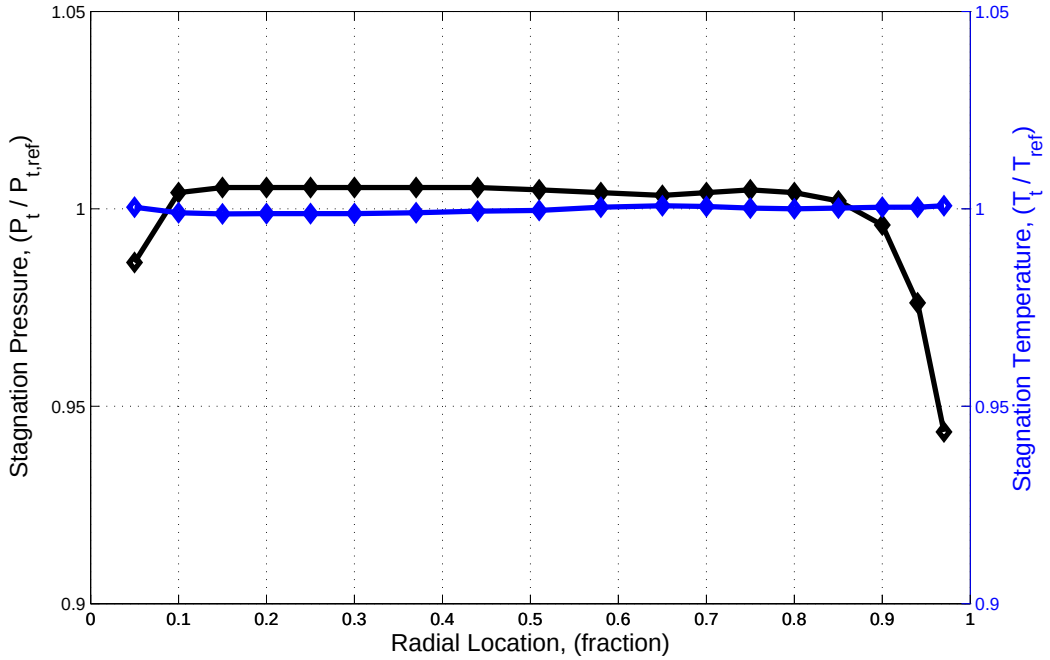

Figure 2-3: Radial profiles of stagnation pressure and stagnation temperature at the computational domain inlet. $p_{ref} = 101325\ [Pa]$, $T_{ref} = 288.15\ [K]$

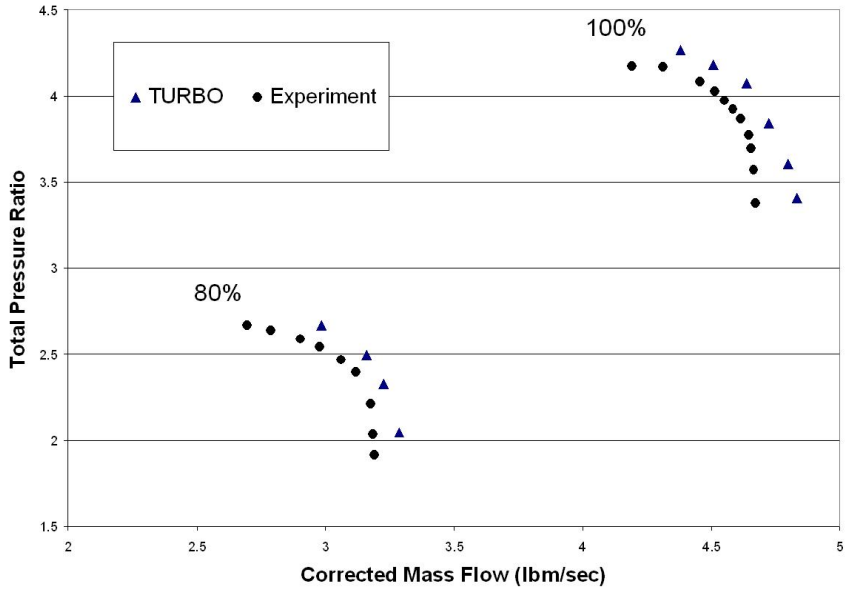

Figure 2-4: Comparison of TURBO results with experiment at 80% and 100% corrected speed

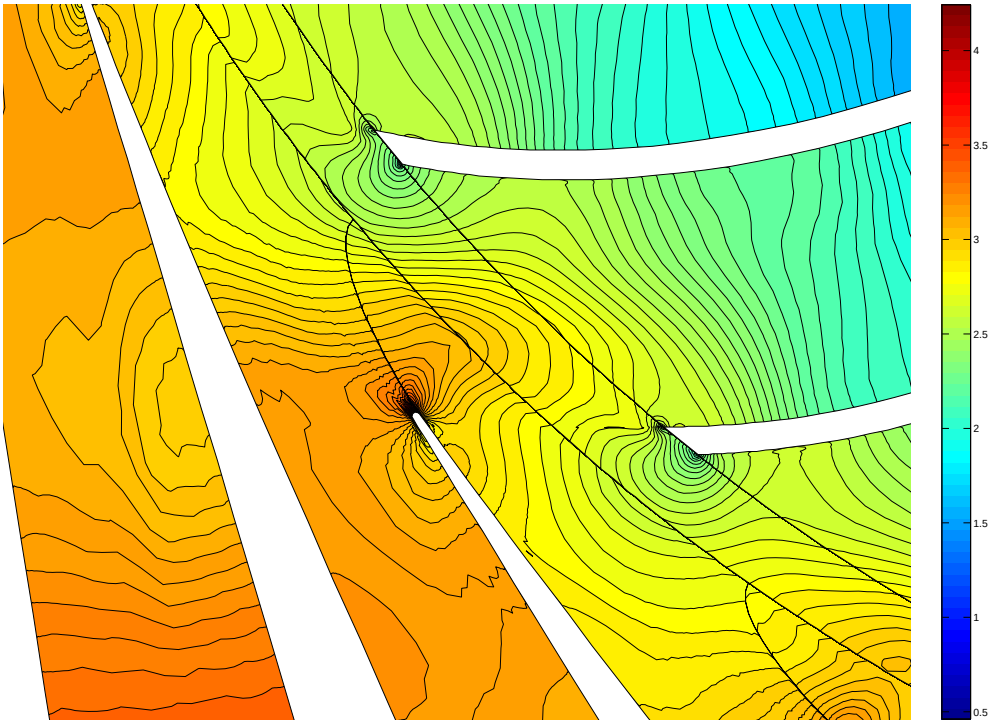

Figure 2-5: Mach related distortion of static pressure isobars, $\frac{p}{p_{t_{ILE}}}$, in CC3 diffuser. $M = .87$, $M_r = .2$

Output Variable	Definition
Q1	$\frac{p}{\rho_{ref} v_{ref}^2}$
Q2	$\frac{\rho}{\rho_{ref}}$
Q3	$\frac{\rho u}{\rho_{ref} v_{ref}}$
Q4	$\frac{\rho v}{\rho_{ref} v_{ref}}$
Q5	$\frac{\rho w}{\rho_{ref} v_{ref}}$

Table 2.1: Output flow quantities from TURBO

$G/S_{_D}$	Impeller Trailing Edge	Diffuser Trailing Edge
VC	0.14%	1.60%
0.28	0.54%	4.81%
0.40	0.73%	0.15%
0.60	0.90%	5.79%

Table 2.2: Discrepancy between entropy rise calculated by integrating the dissipation function to that calculated using state-variables. Quantities expressed are evaluated from the computational domain inlet to the location specified

$G/S_{_D}$	$\Delta r_{_{ITE}}$,(%)	ΔW,(%)	ΔP_t,(%)
0.20	2.24	5.41	6.19
0.24	1.00	2.39	2.71
0.28	0	0	0
0.31	−1.00	−2.37	−2.64
0.40	−3.41	−8.00	−8.69

Table 2.3: Summary of estimated performance changes due to growth/shrinkage in impeller tip radius. Calculated using known flow conditions in the CC3 impeller.

$G/S_{_D}$	$r_{_{DLE}}\,[m]$	Λ
0.28	0.2882	80.30°
0.40	0.2984	80.58°
0.60	0.3168	80.94°

Table 2.4: Summary of vane stagger angle and leading edge radius with gap to pitch ratio

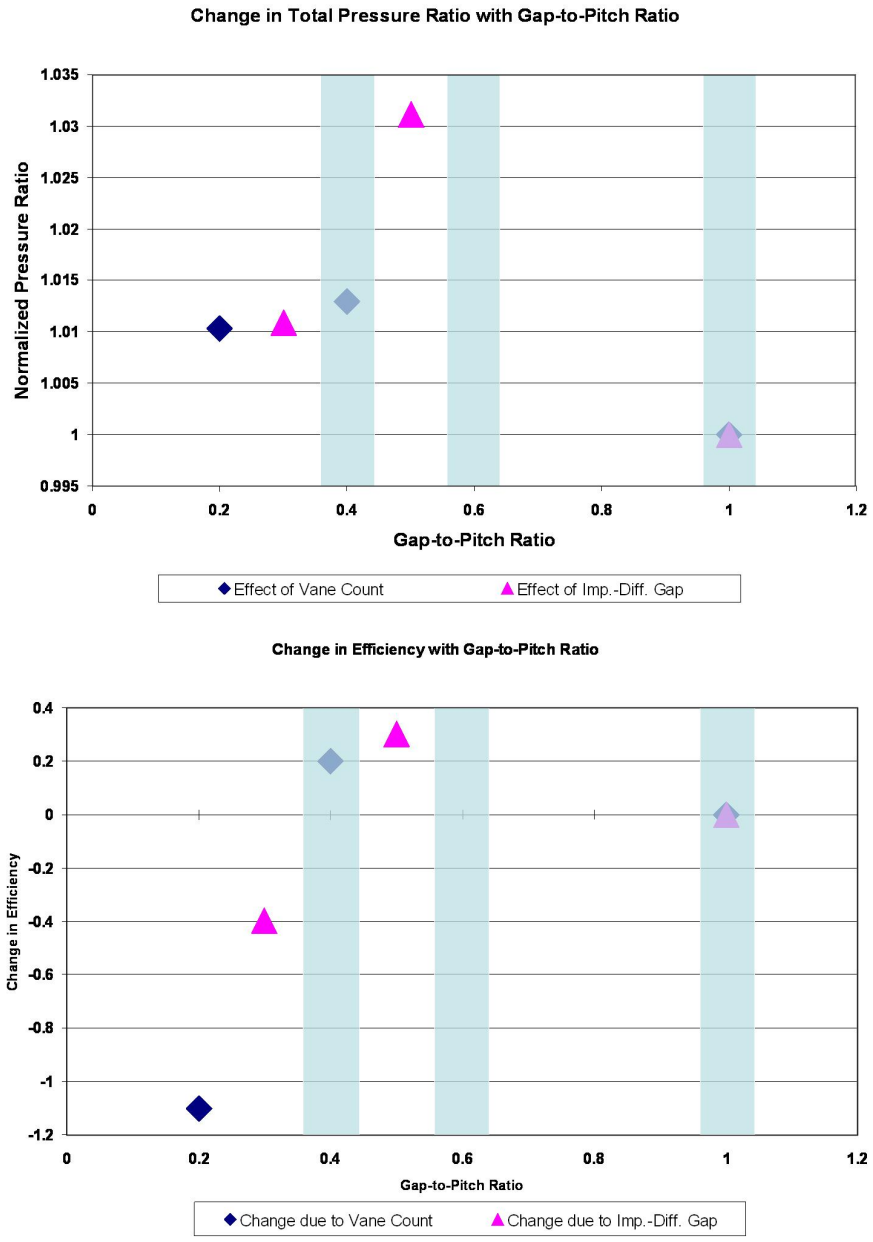

Figure 2-6: Performance data across impeller as a function of G/S_D with current G/S_D targets highlighted

G/S_D	$\overline{\dot{m}}^{t}_{corr,design}$	$\sigma\left(\dot{m}_{corr,design}\right) \times 10^{-4}\ [kg/s]$
VC	4.667 $[kg/s]$	5.4
0.28	$+0.19\%$	3.9
0.40	$+0.09\%$	3.2
0.60	-0.02%	1.9

Table 2.5: Achieved corrected mass flow tolerances for all cases

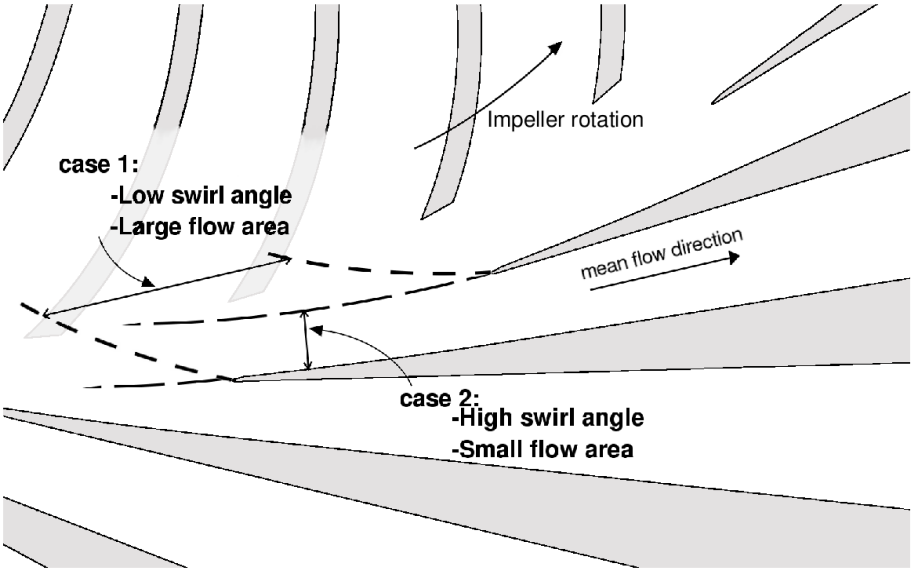

Figure 2-7: A qualitative representation of area change with swirl angle at diffuser leading edge (adapted from [1])

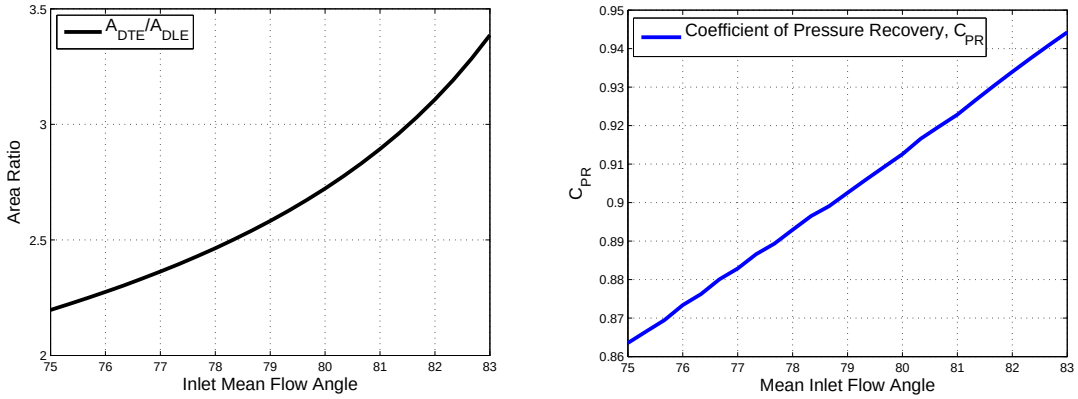

Figure 2-8: Area ratio and coefficient of pressure recovery as functions of flow angle using one-dimensional diffuser model

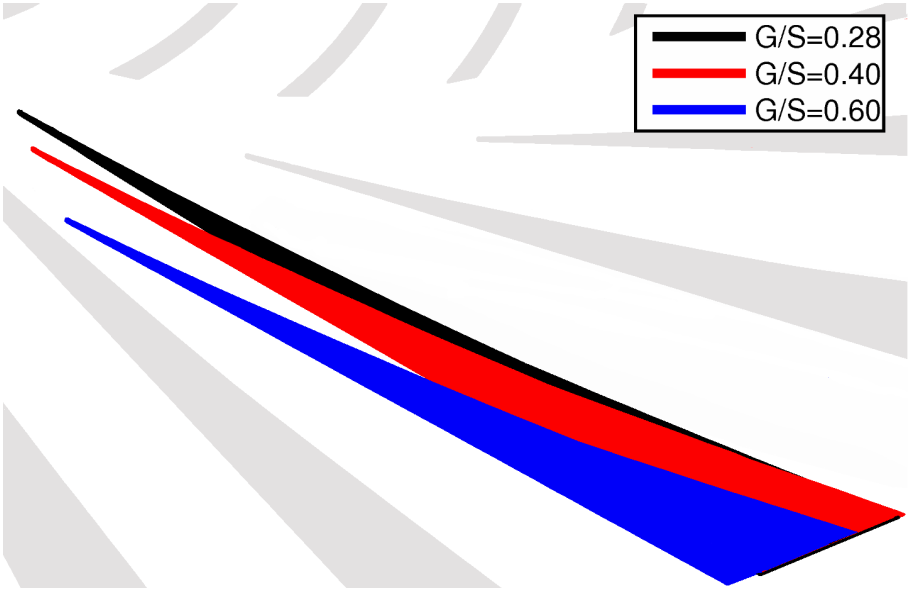

Figure 2-9: Vertical projection of diffuser vanes for $G/S_D = 0.28, 0.4, 0.6$

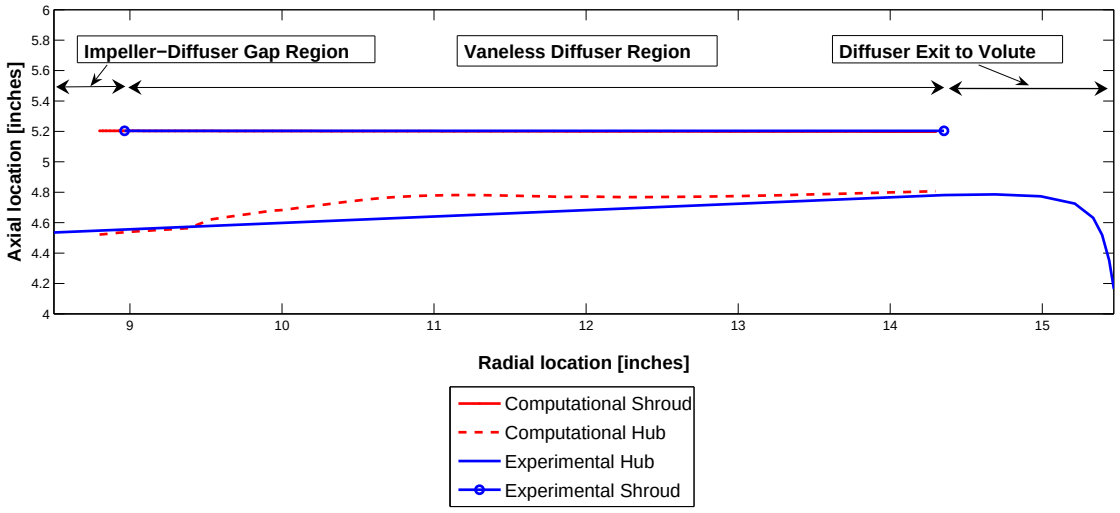

Figure 2-10: Comparison of computational vaneless diffuser depth with experimental rig set up from Skoch,[2]

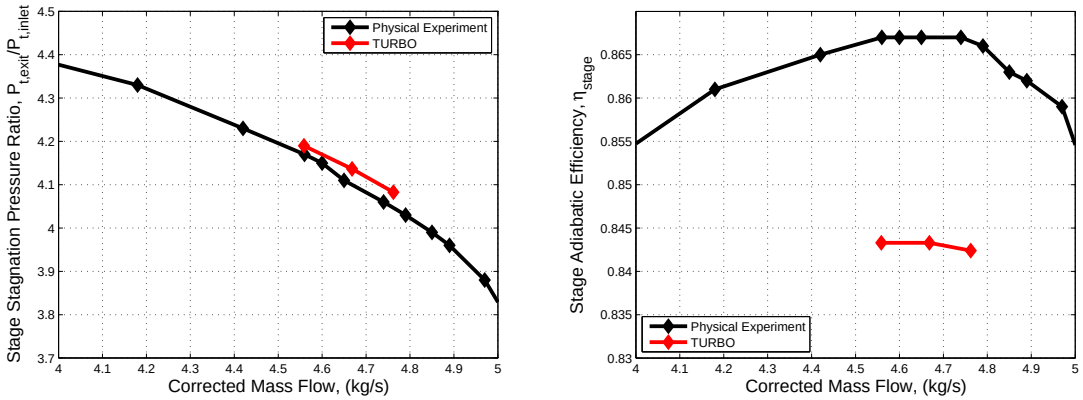

Figure 2-11: Comparison of the time-averaged TURBO results compared to those of the physical experiment conducted by Skoch, [2]. Stage stagnation pressure ratio and adiabatic efficiency shown

Chapter 3

Results

3.1 Introduction

This chapter presents the findings of the computational experiment and quantifies them on a time averaged and unsteady basis. Since the work of Shum and Murray identifies the impeller as the component with the largest performance response to impeller-diffuser interactions, it is the main focus of this chapter. The analytical framework that has been developed to address changes in the impeller is applied to the time averaged data first. The trends and observations of the time averaged investigation, combined with similar observations from Shum and Murray, point to changes in the blade leakage flow as a key component to performance change. From here the unsteady investigation begins followed by the development and use of methods to explain the observations gathered from the data. A more detailed summary of each approach, time averaged and unsteady, is given at the start of the respective sections.

The performance of the diffuser was not assessed because it was found that the incidence angle on the diffuser vane varied by more than $\Delta\left(\Lambda - \alpha_{_{DLE}}\right) = 4^{\circ}$ between cases. The tolerable range of time average incidence angles was estimated to be $\Delta\left(\Lambda - \alpha_{_{DLE}}\right) \leq 1^{\circ}$ by the data from Phillips, [1]. Above this tolerance the performance differences due to interaction could not be separated from performance differences due to the change in loading, boundary layer behavior, or area ratio stem-

ming from incidence angle change. This difficulty is addressed in greater detail in Appendix D.

3.2 Time Averaged Effects

Introduction

To interpret the changes found in the time averaged data, three approaches will be used. The first method is examination of the time and mass averaged performance quantities over the impeller: stagnation pressure ratio and efficiency. The change in time average performance is assessed against the hypothesized trend based on gap to pitch ratio as well as in terms of the time and mass averaged loss profile through the compressor. The difference in loss through the compressor should closely match the trend in efficiency as well as identifying streamwise locations of high loss. Next, impeller channel cross sections (normal to the flow) of entropy production will be examined to identify where in the channel the regions of high entropy production occur (e.g. near the casing, on the pressure side of the blade). These plots of entropy production, or dissipation, will be compared to the vaneless case to highlight differences attributed to interaction effects, and then to similar plots from Shum to gauge the relative magnitude of changes in dissipation due to the effects of impeller-diffuser interaction. Lastly, the one dimensional model developed by Shum will be used to determine the performance change based on the current results. Its effectiveness in estimating the stagnation pressure ratio using the computational data will be evaluated for the CC3. From this estimation, the relative magnitude of the loss, blockage, and slip terms will be used to identify which is producing the largest performance change. Knowing this will help direct the areas of further investigation.

3.2.1 Time Averaged Performance

Once the simulations reach convergence, as defined in section 2.5.4, the solutions are time averaged and evaluated for any macroscopic performance differences between

cases. The key parameters, stagnation pressure ratio and efficiency, are normalized and plotted across the impeller alongside the data from previous experiments (the hypothesized universal curve) in figure 3-1. The differences observed here are displayed numerically in table 3.1 along with other important performance parameters. The changes observed here in the impeller efficiency and stagnation pressure ratio due to interaction are well below those seen by the other studies. In fact, these changes are below the tolerance specified in section 2.5.4 for which we can separate performance changes due to interaction from those due to mass flow variation on the compressor speedline. Therefore, given the operating conditions used in this study, no significant performance change has occurred due to impeller-diffuser interaction in the CC3.

The plot of the time and mass averaged loss through the compressor domain, shown in figure 3-2, supports this observation. In contrast to Shum and Murray's conclusions, the significant differences in loss occur in the diffuser and in the vaneless region whereas entropy production in the impeller is not discernably different from case to case.

It is expected that the unsteady pressure disturbance produced by the diffuser, as viewed from the reference frame of the impeller, would cause noticeable changes to the flow field. The reason why it does not result in time averaged performance changes is the focus of the rest of this investigation.

3.2.2 Dissipation

The rate of entropy production not only determines the entropy flux at the impeller exit, but also directly affects the impeller stagnation pressure ratio. We expect the largest unsteadiness to be present at the impeller location nearest to the diffuser, as equation 2.3 suggests, therefore the meridional plane of 99% impeller chord is chosen for evaluation. Because the largest unsteadiness occurs here, the results from this location will highlight the regions most influenced by interaction and provide an upper bound on the dissipation changes due to interaction in the impeller.

Using equation 2.34, the rate of entropy production is time and volume averaged so that comparison of entropy generation rates between cells of different volumes is

meaningful. The difference in the local entropy production rate between the vaneless case and each of the vaned cases is then taken at the meridional plane of 99% impeller chord. These differences are then each normalized by the mean volumetric dissipation across the vaneless case's corresponding meridional plane. The result is a quantified change in entropy production rates relative to the vaneless case (zero interaction), and due to varying levels of interaction. Results for all cases are displayed in figure 3-4. As a reference, the volumetric dissipation rate for the vaneless case itself, $\frac{T_{ITE} S_I \left(\rho \frac{Ds}{Dt}\right)}{\frac{1}{2}\rho_{ITE} U^3}$, is provided in figure 3-3.

The maximum and minimum values on the scale, 1 and -1, represent a 1x and -1x change from the vaneless case, or 100%. To complement the graphical representation of dissipation, table 3.2 presents the maximum, minimum, mean, and standard deviation values of the data for all cases. When these results are compared to the equivalent calculations from Shum's experiment, the current data falls an order of magnitude below the values he observed. In the corner of the casing and suction surface, he recorded peak values from 100x to 200x and saw extended regions of -4x to -8x. The current data sees values which are much smaller, with maximums between 4x to 16x and extended regions of roughly -0.5x. Also, the values here occur in small, isolated pockets whereas the regions of high relative dissipation extend across significant portions of the channel pitch in Shum's data. The figures from Shum are provided in figure 3-5 for comparison.

These plots of time average dissipation relative to the vaneless case show that changes in the blade leakage flow with increasing interaction do not dominate the entropy production in the CC3. The change is so small that for the case of highest interaction, $G/S_{_D} = 0.28$, the change in shear layer entropy generation near the walls is of the same order of magnitude as that of the blade-leakage flow. This result, that the change in dissipation of the blade leakage flow is not the primary change due to interaction, is in contrast to the findings of Shum and Murray. Therefore, the observed change in blade leakage dissipation due to interaction could be the cause of the small changes in performance that the time averaged data shows.

To seek possible explanations for this unexpected behavior, we turn to the one

dimensional model developed by Shum that identifies the individual contributions of loss, blockage and slip to estimate stagnation pressure change. If the model captures the performance trend of the time averaged data, the contribution of each term may help identify the reason why no sizeable change in performance occurs with varying degrees of interaction.

3.2.3 Application of Shum's One Dimensional Model for Impeller Performance

Shum identified three primary factors that reflect changes in impeller performance associated with interaction effects: loss, blockage and slip. A measure of each of these should provide us some insight as to how interaction is affecting the impeller. Table 3.3 shows the values from the present computations that are used in Shum's one-dimensional approximation. Evaluation of these quantities is conducted at the impeller trailing edge plane. Unlike entropy and slip angle, no absolute blockage value is calculated because the method used only quantifies relative changes. This method is described in detail in Appendix B. These values are then applied to Shum's one-dimensional model along with the influence coefficients (see section 2.6.2), which are calculated directly using quantities from the numerical solution.

The results from the one-dimensional model, figure 3-6, show that the trend is qualitatively similar for the static and stagnation pressure with the exception of $G/S_{_D} = 0.40$. Quantitatively, the difference between the two models is large, especially for the static pressure, and the difference increases with increasing interaction. Such a large discrepancy between the results of the one-dimensional model and the numerical simulation is not seen in Shum's study [3]. This large discrepancy between the results from TURBO and the one dimensional model might be a result of the small magnitude of changes here relative to the performance changes in Shum's experiment. It is possible that when such small changes in performance exist, the coefficients of the one dimensional model may need to be refined to more adequately reflect the changes in slip, loss, and blockage. However, for the purposes of this study, it is deemed more

important to determine the causality of the small performance changes.

Despite the quantitative discrepancies, the simplified model does capture the scaling of stagnation pressure change between $G/S_{_D} = 0.28$, $G/S_{_D} = 0.60$, and the vaneless case. Examination of the individual contributions of loss, blockage and slip to the performance change estimated from the one dimensional model for these gap to pitch ratios is then used to guide the next step of the investigation. Table 3.4 indicates that the largest changes in stagnation pressure come from the blockage term for $G/S_{_D} = 0.60$, and from the loss and blockage terms for $G/S_{_D} = 0.28$. Murray and Shum found that these two effects are driven primarily by the unsteady characteristics of flow leaking through the gap between the impeller blade and the casing. This flow will henceforth be referred to as blade leakage flow, and quantities pertaining to this flow through the blade-casing gap will have the subscript "BCG".

3.3 Unsteady Effects

Introduction

To determine whether the unsteady pressure field from the diffuser is propagating into the impeller, and with what strength, we begin by characterizing the level of unsteadiness in the impeller passage. We then look at whether or not this unsteadiness translates into an unsteady blade loading and its corresponding blade leakage mass flux, and compare these values to those seen in Shum's study. Doing this reveals that the ratio of unsteady amplitude to the time averaged value of blade leakage mass flux is much higher for Shum; this ratio, $\Delta w_{_{BCG}}/\overline{w}^{\mathbf{t}}_{_{BCG}}$, is henceforth referred to as the relative unsteadiness parameter.

At this point in the analysis it is decided to decompose the mixing out process between the blade leakage flow and the main passage flow into two components: the sudden expansion of the blade leakage flow, and the mixing of the main flow. Their sum is equivalent to the mixing out process that would take place between these two intersecting streams.

The first component is used to develop a simplified one dimensional model, based

on the relative unsteadiness parameter, for estimating losses in the blade leakage fluid due to unsteady velocity fluctuations. Application of this model shows that Shum's machine would yield additional loss due to unsteadiness in the blade leakage fluid that is five to thirty percent of the steady-flow dynamic head larger than the CC3.

The second component employs a model developed by Denton, [22], that captures the loss in the main passage fluid due to mixing, and does not account for loss in the jet (blade leakage) fluid. Together these two components form what is henceforth referred to as the 'loss potential model'.

The results of the loss potential model are compared to the mixed out results of the computational flow field and found to adequately capture the loss potential in the blade leakage region. Since we have shown that the dissipation in the blade leakage region is not the dominant loss mechanism due to interaction for the passage cross section in section 3.2.2, we compare the *potential* for loss in the blade leakage region to the other regions of the passage cross section. This way, we can attribute the source of loss potential to the region in which the flow nonuniformity is created even if it convects to another region before mixing out. Carrying this analysis out, we find that the loss potential in the blade leakage region is of the same magnitude as the other cross sectional regions. With this knowledge we can say that changes in the blade leakage flow due to unsteadiness neither have a strong effect on loss production (dissipation) nor on the potential for loss. Thus, it can be concluded that changes in blade leakage flow have a small effect on performance change due to interaction, unlike what has been observed in previous studies.

3.3.1 Passage Unsteadiness

To determine the potential to which unsteady interaction effects may be altering performance, specifically through the blade-casing gap, we must know the extent to which the unsteady pressure field propagates into the impeller and its strength. To quantify this the standard deviation of pressures through the centerline of the impeller channel are plotted in figure 3-7 over one blade passing period for each gap to pitch ratio. This will henceforth be referred to as the 'unsteadiness level' in the impeller.

It can be seen that the largest differences in unsteadiness occur in the last 10% of the channel and the amplitude of unsteadiness scales with decreasing G/S_D ratio. This result indicates that we should expect some performance differences due to the varying degrees of interaction.

When compared with the unsteadiness data from Shum, the unsteadiness level for all of the present gap to pitch ratios is less than Shum's $G/S_D = 0.50$ case [1]. Although we have no configuration of $G/S_D = 0.50$, the trend of our data would indicates that it would lie between that of $G/S_D = 0.40$ and $G/S_D = 0.60$ at a trailing edge value of just over 1% of the impeller exit dynamic head. This would mean that the unsteadiness level in Shum's impeller is five times larger than that of the current study. An implication of this comparison is that the $p'(0,0)$ term in equation 2.3, which characterizes the pressure disturbance at the diffuser leading edge, may play an important role in setting the strength of interaction. The fact that Shum's observed performance changes with varying degrees of interaction are large, and his passage unsteadiness is large, relative to the current study, is a similarity worth noting. If the losses are shown to be driven by unsteadiness, then difference in unsteadiness levels shown in figure 3-7 suggest that the $p'(0,0)$ term is an important component to describing performance changes due to impeller-diffuser interaction and should not be omitted in any hypothesis to predict its effects.

3.3.2 Blade Leakage Loading and Mass Flux Profiles

With this established we now move to examine the effects of this unsteadiness on the flow in the region of the blade-casing gap. Because of the circumferentially periodic nature of the pressure fluctuations we expect there to be a loading and unloading of the impeller blades as they encounter each pressure front. The loading across the splitter blade in the blade-casing gap region is plotted in figure 3-8 over one blade passing, at three streamwise locations, for all cases. The blade loading completes one

[1] Shum states that his unsteadiness quantification uses the *"[root means square] time fluctuation of static pressure"*. This method is equivalent to the standard deviation of pressure used here, if the root mean square of the pressure perturbation, $(p - \overline{p})$ is used.

cycle over the time of one blade passing, confirming that the unsteadiness is primarily due to the influence of the downstream diffuser vanes.

Two aspects to note are that the amplitude of the unsteady loading diminishes with distance upstream from the impeller trailing edge, and that the mean loading value increases with distance upstream from the impeller trailing edge. The decrease in unsteady amplitude is understood to be a result of the exponential decay as implied in equation 2.3. The explanation for the mean loading decrease toward the trailing edge can be viewed as an effect similar to the Kutta-condition: no static pressure gradient can exist across the straight streamlines leaving the sharp trailing edge. Since the static pressure must be continuous, an adjustment region must occur on the blades where the loading decreases toward the trailing edge. However, since the flow is not steady the Kutta-condition requirement that the stagnation point lie at the sharp trailing edge does not hold and a net loading is possible. Evidence of this is offered in Murray's identification of what he calls "tip flow back leakage", where the stagnation point no longer resides at the blade tip but on the suction side of the blade, leading to increased circulation and loading [8].

For the flow in the blade-casing gap, it follows that the unsteady pressure fluctuation through the blade-casing gap must drive a corresponding mass flow fluctuation. Figure 3-9 plots this corresponding mass flux per unit area through the blade-casing gap, non-dimensionalized by the mass flux per unit area at the impeller exit[2]. The most important observation to make is that the loading profiles are generally in phase with the mass flux profiles, meaning that the mass flux through the blade-casing gap responds almost instantly to the applied loading. This suggests that the process could be approximated as taking place on a quasi-steady basis. Calculating the reduced frequency for the blade-leakage flow will provide us an estimate of the degree to which this is true.

$$\beta_{BCG} = \frac{\Omega N_D \, b_I}{2\pi \, w_{BCG}} \; = \; 0.22 \tag{3.1}$$

[2]Shum's non-dimensionalization is different from what is used here. When comparing the current results to those of Shum, the reader should note this difference. However, it will be shown in section 3.3.3 that the important measure of blade leakage flow as it pertains to loss and blockage (the relative unsteadiness parameter) will eliminate quantification differences due to normalization schemes.

If the reduced frequency were much less than unity, $\beta_{BCG} \ll 1$, it would be a strong indicator that the flow process through the blade-casing gap occurs in a manner largely uninfluenced by unsteady effects. Although the result of equation 3.1 is not close to zero, it indicates that the quasi-steady effects are significantly more important than the unsteady effects for the flow through the blade-casing gap. Using this, we begin our analysis of the flow by making the approximation that the process takes place in a quasi-steady manner.

3.3.3 Quasi-Steady Blade Leakage Model

Blade-Leakage Jet Sudden Expansion Model

Shum's analysis concluded that only the unsteady aspects of blade leakage flow could be responsible for the observed performance change seen in the impeller. However the data presented in section 3.2 shows a contribution of the blade leakage flow to entropy production levels (relative to the vaneless case) that is an order of magnitude lower than what Shum observed. To understand why this large disparity exists between these two compressors, a simple model is sought to understand the flow processes that govern loss generation in blade leakage flow.

One difference that is noticed between Shum's data and the current data is that the amplitude of Shum's unsteady blade leakage mass flux profiles relative to their mean value is larger than the same measure of the profiles presented in figure 3-9. To understand what effect this may have on the flow through the blade gap we can use the approximation that the blade leakage flow is quasi-steady to estimate the loss. If we consider the fluid exiting the blade-casing gap to be akin to a jet exiting into a larger channel, as depicted in figure 3-10, we can use the conservation of mass, momentum, and energy to calculate the stagnation pressure drop due to mixing as a function of the inlet jet velocity and the area ratio between the jet and the channel. The result for a low Mach number, steady inlet velocity is:

$$\Delta p_{t,steady} = \frac{1}{2}\rho\left(1 - \frac{A_1}{A_2}\right)^2 w_1^2 \tag{3.2}$$

Since the area ratio is very small (i.e. $A_1/A_2 \ll 1$) and constant for the current application ($A_1/A_2 \approx 0.02$), this term will be omitted in the rest of the analysis for simplicity.

With the approximation that the flow process through the blade-casing gap is quasi-steady, the instantaneous stagnation pressure change of the fluid jet, Δp_t, can be calculated based on the instantaneous inlet velocity using equation 3.2. These values are calculated at every infinitesimal time increment, dt and integrated over one period of inlet velocity unsteadiness to find the average stagnation pressure decrease. The effect of the unsteadiness on the stagnation pressure change can be seen from analyzing a simple square wave, shown in figure 3-11. Because the stagnation pressure drop depends on the square of the inlet velocity, the contribution of the $(w + \Delta w)$ term is not balanced by that of the $(w - \Delta w)$ term, and there is a net increase in the stagnation pressure drop due to the unsteady inlet velocity.

$$\frac{\overline{\Delta p_t}^{\mathbf{t}}}{\frac{1}{2}\rho\overline{w_1}^2} = \frac{1}{2}\left(1 + \frac{\Delta w}{\overline{w_1}}\right)^2 + \frac{1}{2}\left(1 - \frac{\Delta w}{\overline{w_1}}\right)^2 = 1 + \left(\frac{\Delta w}{\overline{w_1}}\right)^2 \tag{3.3}$$

Taking the difference of equations 3.2 and 3.3 yields the difference in stagnation pressure change due to an unsteady, square wave velocity profile:

$$\frac{\overline{\Delta p_t}^{\mathbf{t}} - \Delta p_{t,steady}}{\frac{1}{2}\rho\,\overline{w_1}^2} = \left(\frac{\Delta w}{\overline{w_1}}\right)^2 \tag{3.4}$$

The difference in the stagnation pressure change is a quadratic function of the relative unsteadiness parameter, $\Delta w/\overline{w_1}$, where Δw is the amplitude of the unsteady velocity fluctuation. This quadratic dependence on the relative unsteadiness parameter holds true for velocity profiles which are periodic with time.

In steady, adiabatic flows we can calculate the lost work, rather than simply the stagnation pressure drop, using Gibbs' equation in terms of stagnation quantities. The result is equation 3.5, which represents the loss due to the mixing out of the jet as it expands into the channel as a fraction of the inlet kinetic energy. A similar approach to that used in arriving at equation 3.4 yields equation 3.6, which gives an

expression for the increase in loss associated with an unsteady velocity fluctuation relative to that of a steady profile for two jets with the same time average inlet velocity. Both of these equations make no assumption about the magnitude of the entropy change or the Mach number at which they occur.

$$\frac{T_t \Delta s}{\frac{1}{2} w_1^2} = \frac{c_p T_t}{\frac{1}{2} w_1^2} \ln\left(1 + \frac{\gamma - 1}{2} \overline{M_1}^2\right) \tag{3.5}$$

$$\frac{T_t \left(\overline{\Delta s}^{\mathbf{t}} - \Delta s_{steady}\right)}{\frac{1}{2}\overline{w_1}^2} = \frac{c_p T_t}{\frac{1}{2}\overline{w_1}^2} \ln\left[\frac{\left(1 + (\gamma - 1)\overline{M_1}^2 \left(1 + \left(\frac{\Delta w}{\overline{w_1}^{\mathbf{t}}}\right)^2\right) + O\left(\overline{M_1}^4\right)\right)^{1/2}}{1 + \frac{\gamma - 1}{2}\overline{M_1}^2}\right] \tag{3.6}$$

For low Mach number flow ($M_1 \ll 1$) the expressions shown in equations 3.5 and 3.6 respectively reduce to:[3]

$$T_t \Delta s = \frac{-\Delta p_t}{\rho_t} \qquad \rightarrow \qquad \frac{T_t \Delta s}{\frac{1}{2} w_1^2} = 1 \tag{3.7}$$

$$\frac{T_t \left(\overline{\Delta s}^{\mathbf{t}} - \Delta s_{steady}\right)}{\frac{1}{2}\overline{w_1}^2} = \left(\frac{\Delta w}{\overline{w_1}^{\mathbf{t}}}\right)^2 \tag{3.8}$$

These expressions are the tools we will use to estimate the loss of a jet undergoing sudden expansion and to characterize the increased loss due to quasi-steady velocity fluctuations. We will use them to evaluate the current blade leakage data and the data available from Shum's work, to determine if the unsteadiness translates into a much higher loss for Shum's compressor than for the CC3.

Figure 3-12 plots the result of applying equation 3.6 for Shum's data and the current data at three meridional locations, 90%, 95%, and 99% impeller chord, and for four G/S_D ratios. The computed increase in loss due to unsteadiness computed

[3]For Mach numbers less than $\overline{M}_1^{\mathbf{t}} = 0.4$ and $\Delta w / \overline{w}^{\mathbf{t}}$ less than 1, both of these approximations have errors of less than 5% from the exact equations (3.5, and 3.6)

here is $5\% - 30\%$ of the steady dynamic head larger for Shum than for any of the current data. It also does not directly scale with G/S_D ratio, as we would expect it to if hypothesis put forward by Murray were true.

The finding that the loss in the leakage flow is much lower here than in Shum's study is also in agreement with the dissipation plots of figure 3-4. When viewed on this basis, this reasoning offers an explanation as to why the blade leakage flow has such a strong effect on the performance of Shum's impeller, and not such a strong effect here. It also provides the first connection between the level of unsteadiness in the impeller and performance loss, indicating that Murray's hypothesis, stated in section 1.1 may not be correct and that the magnitude of the unsteady pressure needs to be included in the hypothesis.

In addition to the mixing loss due to sudden expansion of the blade leakage jet, the entropy generated from the blade leakage jet intersecting and mixing with the main channel flow is also an important loss mechanism in the blade leakage region. This process is addressed in the next section.

A Model for Estimating Loss Potential in Blade Leakage Flow

As mentioned above, the jet expansion model does not account for loss due to stream mixing between the blade leakage jet and the main passage flow. Also, we cannot be certain of the manner in which the mixing process occurs. It is possible for the flow nonuniformity introduced in the blade-leakage region to convect to a different region of the passage before mixing out. Because of this possibility, the blade leakage flow may still be an important source of performance loss if the mixing process takes place elsewhere in the compressor. To address this, we aim to quantify the *potential* for loss in the blade-leakage region, which will give the upper bound of the loss that could be produced, even if the flow nonuniformities were to mix-out in a different location. To do this, and to account for the stream mixing between the main passage flow and the blade leakage flow, a mixed out averaged model for stream mixing is used.

A model for the mixing process between two intersecting streams has been developed by Denton [22]. This quasi-one dimensional model, given in equation 3.9 below,

evaluates the mixed out entropy rise for two streams intersecting at an angle with different streamwise velocities and different stagnation temperatures. It is the direction of the flow with the higher mass flux which defines the streamwise direction. One stream is assumed to have much smaller mass flow than the other, $d\dot{m}$ versus $\dot{m}$, such that the entropy rise of the smaller, injected stream is insignificant compared to the total specific entropy rise of the combined streams. As shown by equation 3.9 below, the specific entropy rise of the main flow is dependent on the velocity components in the streamwise direction, the relative amount of injected mass, the relative stagnation temperatures, and the Mach number.

$$\frac{ds}{c_p} = \frac{d\dot{m}}{\dot{m}} \left[\left(1 + \frac{\gamma - 1}{2} M^2 \right) \left(\frac{T_{t_{inj}}}{T_t} - 1 \right) + (\gamma - 1) M^2 \left(1 - \frac{w_{x_{inj}}}{w_x} \right) \right] \tag{3.9}$$

It is important to reiterate that the assumptions of this model exclude any specific entropy rise of the injected fluid, therefore the specific entropy change represented in equation 3.9 is due to the mixing of the fluid in the main channel only, even though the mixing itself occurs due to the nonuniformity introduced by the injected fluid. Since the specific entropy rise of the blade leakage fluid is not included in this model, it can be accounted for by adding equation 3.5 to Denton's model and multiplying by the ratio of mass flows, $d\dot{m}/\dot{m}$. This approximation will hold as long as $d\dot{m}$ is significantly less than $\dot{m}$, otherwise the mixing expression must be derived again. The sum of this term with Denton's model, non-dimensionalized in the manner of equation 3.5, will henceforth be referred to as the 'loss potential model'. The form of the loss potential model that will be used in later analysis is written in terms of the impeller relative Mach number for the blade leakage flow.

$$\frac{T_t\, ds}{\frac{1}{2}U^2} = \frac{T_t\, c_p}{\frac{1}{2}U^2} \frac{d\dot{m}}{\dot{m}} \left[\left(1 + \frac{\gamma - 1}{2} M_{_{BCG}}^2 \right) \left(\frac{T_{t_{inj}}}{T_t} - 1 \right) + (\gamma - 1) M_{_{BCG}}^2 \left(1 - \frac{w_{_{MFD,inj}}}{w_{_{MFD}}} \right) \right.$$

$$\left. + \quad \ln \left(1 + \frac{\gamma - 1}{2} M_{_{BCG}}^2 \right) \right] \tag{3.10}$$

3.3.4 Mixed Out Loss Potential

Introduction

The expression encapsulated in equation 3.10 provides a direct estimate of the total loss potential of the blade leakage flow to which the computational results from TURBO can be compared. First, the loss potential of each case is evaluated using the mixed out averaging method described in section 2.6.1 on the computational data from TURBO. Any differences in the time averaged loss potential may point to the existence of nonuniformities introduced by impeller-diffuser interaction that could result in performance change.

First, it is of technical interest to identify what regions in the compressor contribute the most to the loss potential. For this, the impeller passage cross section is divided into regions for which a mixed-out analysis is conducted. These results are then assessed to determine which region is the dominant region. In the region of the blade-casing gap, the loss potential model of equation 3.10 is evaluated for its accuracy in estimating loss potential versus the computational results. The results of this evaluation serve to determine the utility of the model as well as the role of flow processes in each region of the channel cross section in contributing to the overall loss potential of the channel.

Approach to Quantifying Sources of Loss Potential

The term 'loss potential' is used to describe the specific loss increase as the flow settles from the current, non-uniform state to that of the mixed out state. The term 'potential' is used because the mixed out value assumes the mixing process continues at constant flow area until a uniform state is reached while the mass flux, linear momentum, angular momentum, and energy are conserved. Because the mixing out process rarely occurs to completion, the mixed-out results should be viewed as an upper bound for the additional loss due to the nonuniformities present in the flow field.

The mixed out analysis described in section 2.6.1, is used here to compare the spe-

cific loss potential between two channel cross section planes at any arbitrary streamwise impeller location. As the distance between evaluation planes increases, the contribution of the observed entropy production between planes to the mixed out entropy difference also increases. Since the goal of this analysis is to highlight differences in loss *potential* in the flow between two adjacent planes of the impeller channel cross section, the loss potential is calculated as the difference between the mixed out and the mass-averaged local specific entropy values.

$$\xi = \frac{T_{_{ITE}}}{\frac{1}{2}U^2}\left(\bar{s}_i^{\mathbf{X}} - s_i^{\mathbf{M}}\right) \tag{3.11}$$

Figure 3-13 shows the loss potential in one impeller passage for all four gap to pitch ratios and at meridional locations of 90%, 95%, and 99% impeller chord. The time averaged loss potential does not vary significantly from case to case, but the unsteady level of loss potential at each time instant over the blade passing period does. At 99% impeller chord, the large amplitude of the loss potential over the blade passing period indicates that unsteady processes play a role in setting the level of loss potential in the channel at each time instant. Despite this, the mean values for all cases are still roughly equivalent. In contrast to the quadratic effect of velocity unsteadiness on loss discussed earlier, the time average of the loss potential variation over the blade passing is equal to the time average of a steady loss potential. The important feature of this plot is that the time averaged loss potential for all levels of interaction is nearly the same.

The comparison of loss potentials has shown that there is only a small loss potential variance between cases. This small variance is evaluated across the entire passage, and therefore leaves open the possibility that the loss potential is a result of an increased loss potential in one region and a decreased loss potential in another. To address this possibility, and to gain knowledge of the loss potential profile, the channel cross section is divided into five regions selected to coincide with areas of high dissipation as identified in figure 3-4(a). The regions begin with the suction side blade leakage region, $R1$, and are numbered counter clockwise around the channel

(see figure 3-14). If the increase in loss potential in any region is much larger than the loss potential in the other regions, it will be necessary to conduct a sensitivity study on the selection of the regions. The following list identifies the region name and the associated type of loss that is expected to dominate in that region.

- Region $R1$ - blade leakage jet entering channel
- Region $R2$ - blade leakage exiting channel
- Region $R3$ - pressure side boundary layer
- Region $R4$ - center of channel
- Region $R5$ - suction side boundary layer / tip leakage back flow [8]

If mechanisms similar to those that caused performance changes in Shum's and Murray's impellers are occurring here, the loss potential of region $R1$ will be dominant over a small change in meridional location, δi [4]. Also, in region $R1$ the loss potential model should provide a good estimate of the mixed out specific entropy in that region. However, if the loss potential in other regions are of equal or greater magnitude than that in $R1$, then a different loss mechanism is driving the performance loss of the CC3 impeller.

Assessment of the Blade Leakage Model for Loss Potential

The first objective is to determine the applicability of the loss model relative to Denton's model and the computational results. Since the center of $R1$ is one quarter of a passage from the blade, where the data for the one dimensional model is collected, we expect there to be a phase difference between the computational results and the one dimensional model results. This difference is expected to be at least one quarter of a blade passing plus the transit time of the blade leakage jet nonuniformity to the

[4] A small change in meridional location, δi, is selected to isolate the loss potential contributions of a specific region. If a larger distance between evaluation planes were chosen, the nonuniformities evaluated at the upstream plane would have increased opportunity to convect to different regions before reaching the downstream plane, giving a false indication of where loss potential sources reside in the channel

center of $R1$. Knowing the mean velocity of the blade leakage flow, as well as other pertinent details about the compressor, we can estimate that this phase shift should be roughly ~ 0.5 blade passings for $R1$.

Figure 3-15 shows the result of the mixing out process conducted in $R1$ on the computational data from TURBO alongside Denton's estimate and the loss model's estimate. The time averaged loss potentials are shown as thin horizontal lines on the plot. From visual inspection, we see that the phase shift at 90% and 95% is ~ 0.4 blade passings, within 10% of a blade passing of our estimate. However, this phase difference proves to be immaterial when considering the time average loss potential.

The inclusion of the loss in the blade leakage fluid yields a time average loss potential estimate close to that of the calculations. Although the blade leakage fluid accounts for only 5% of the total mass flux in $R1$, it contributes roughly 20% to the estimate of the increase in loss potential. At 99% impeller chord, the model breaks down as the magnitude of the blade leakage flux diminishes, and effects from the impeller blade tip become important (e.g. boundary layer separation, tip leakage back flow) become important. The similarity in magnitude and expected phase-shift for the 90% and 95% chordal locations confirms that the leakage flow dominates the flow field in the corner of the casing and suction side of the impeller blade, as the dissipation plots of figure 3-4 suggest. A similar trend can be observed in figures E-1 and E-2 in Appendix E, for $G/S_{_D} = 0.40$ and $G/S_{_D} = 0.60$, respectively.

The loss potential model used in this analysis has been shown to provide an an adequate estimate of loss potential increase in the region of the casing-suction side corner. This adequacy is expected to hold for most compressors with similar time averaged blade leakage mass fluxes. The reason for this is explained by Denton, [22], when he states that mixing of a jet entering at 90° to a channel realizes nearly all of its potential entropy production within several diameters of the injected jet when mixed with five times its own mass flow [22]. Although not entering at 90°, the injected mass flow from the blade-casing gap is 5% of the channel mass flow in $R1$. Therefore, the mixing process is not limited by the mass flow of the channel and will realize nearly all of its loss potential in a small region near the jet. The plots of dissipation,

figure 3-4, show this rapid mixing of the leakage jet to occur in the CC3 impeller, as do Shum's plots of high relative dissipation in figure 3-5, for his compressor. These arguments justify the omission of the area ratio term, since mixing of the leakage fluid effectively carries to completion in the casing-suction side corner.

Comparison of Loss Potential Increase Between Regions

Now that the loss model has been shown to adequately capture the mixed out loss potential in region $R1$, we can conduct a mixed-out analysis on the computational data from TURBO to evaluate the other cross sectional regions and gauge the relative magnitudes of their increased loss potentials. In conducting this analysis it is important to note that the mixed out conditions from each region cannot be directly compared to one another because the initial conditions (mass flux, momentum, energy) vary slightly from region to region. Between regions the standard deviation of momentum and stagnation temperature are both $\sim 4\%$ of their mean values across the channel. However, we expect to find increases in specific loss potential in $R1$ ten or more times larger than in $R2$-$R5$ if dominant mechanisms similar to those observed in Shum's and Murray's experiments are present. For this purpose the variations in conditions across the channel plane are deemed low enough to be acceptable. Additionally, since we are calculating a mass-flux specific quantity, the value of each region is normalized by the ratio of mass flux through the region itself to the mass flux of the channel. Doing this yields specific entropy values that can be compared to those of other regions. Figure 3-16 plots all of these regions over one representative blade passing for $G/S_{_D} = 0.28$ at three meridional locations. The phase shifts between each region at each meridional location are due to the effect described previously.

When the increase in loss potential from $R1$ is compared to that of the rest of the channel, we find that the change in loss potential of region $R1$ over δi is roughly equal to the change in loss potential of other regions.This means that for the CC3, at the selected operating conditions, there is no dominant source of loss potential due to interaction in the impeller. Similar results for $G/S_{_D} = 0.40$ and $G/S_{_D} = 0.60$ can be found in Appendix E, figures E-3 and E-4, respectively.

3.3.5 Summary of Unsteady Investigation

From the analysis above we can infer that there is no dominant, unsteady loss production mechanism in the impeller. The focus of this evaluation has been on the unsteady blade leakage flow, which produced changes in the time average flow blockage and loss generation that led to measurable performance changes associated with unsteady impeller-diffuser interactions in previous studies ([3], [8]). Under the conditions for which the computations have been carried out both the time averaged entropy generation (dissipation) and the potential for loss have been evaluated. Both analyses show that changes in the blade leakage flow have a minimal effect on changes in CC3 performance with varying degrees of interaction.

The relative unsteadiness of the blade leakage flow, $\frac{\Delta w_{BCG}}{\overline{w}_{BCG}}$, has been shown to be a parameter which appears to characterize the unsteady loss from blade leakage flow. Based on the present analysis, it appears that it is also a parameter which offers an explanation of the observed difference in loss between the CC3 and Shum's compressor.

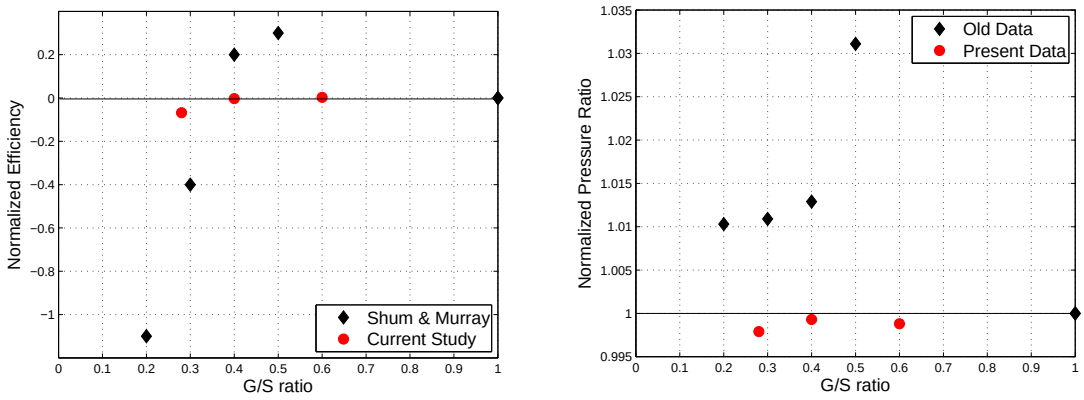

Figure 3-1: Comparison of previous and current performance data across impeller as a function of G/S. All values normalized with the vaneless case

	$G/S = 0.28$	$G/S = 0.40$	$G/S = 0.60$	$Vaneless$
$\Delta \dot{m}_{corr}$	0.23%	0.09%	−0.02%	4.652 $[kg/s]$
$\Delta \frac{p_{t,ITE}}{p_{t,ILE}}$	−0.17%	0.01%	−0.05%	4.138
$\Delta \frac{p_{ITE}}{p_{t,ILE}}$	0.60%	0.76%	0.69%	2.672
$\Delta \frac{w_{tan,ITE}}{U_{ITE}}$	−0.087%	−0.023%	−0.043%	0.697
$\Delta \eta$	−0.075%	−0.0113%	0.005%	0.931

Table 3.1: Summary of impeller performances relative to vaneless case

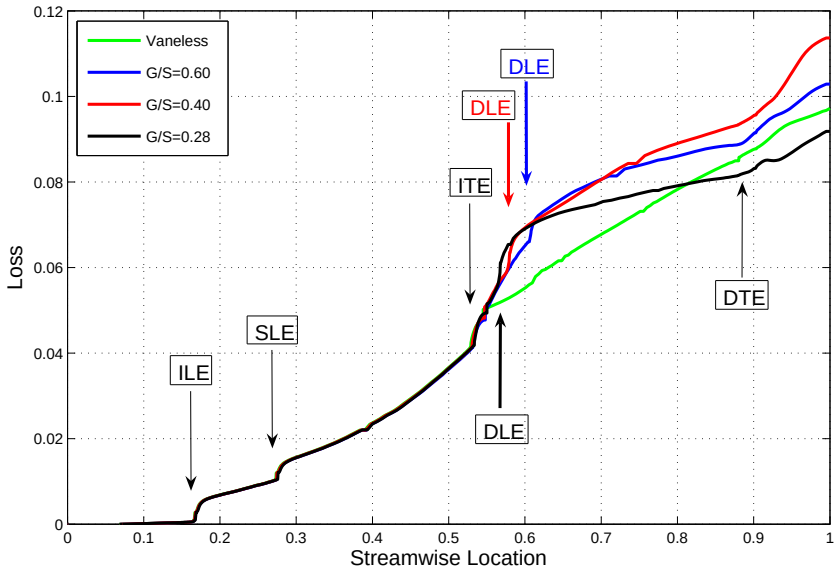

Figure 3-2: Time and mass-averaged loss, $\frac{T_t \Delta s}{\frac{1}{2}U^2}$, measured relative to the impeller inlet in the streamise direction through the CC3

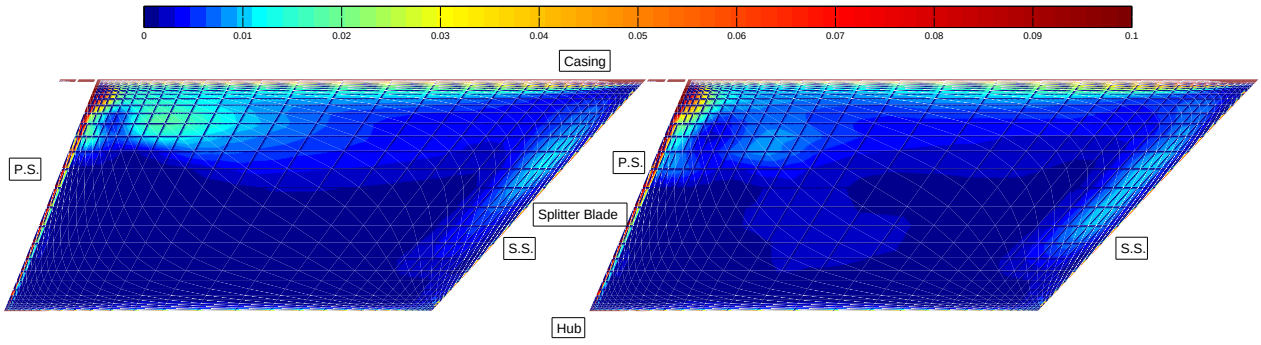

Figure 3-3: Dissipation profile for the vaneless case, 99% impeller chord, $\frac{T_{ITE} S_I \left(\rho \frac{Ds}{Dt}\right)}{\frac{1}{2}\rho_{ITE} U^3}$

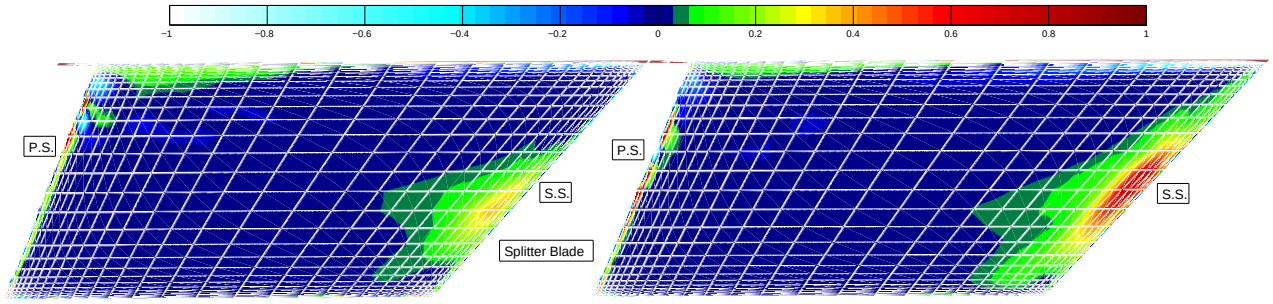

(a) $G/S = 0.28$

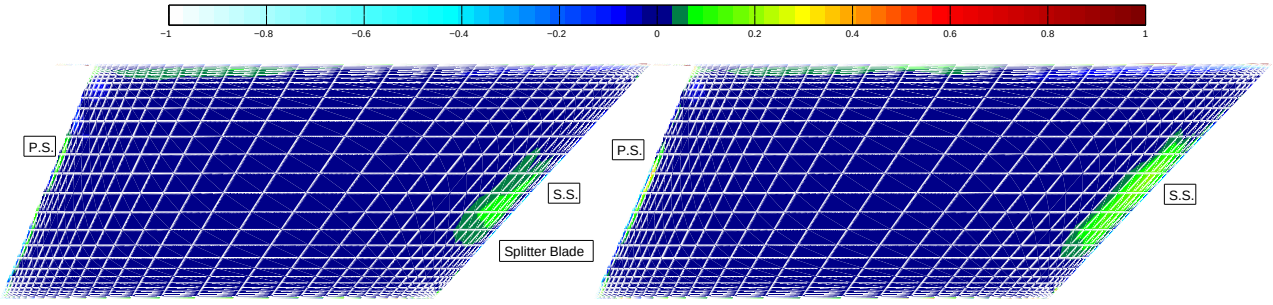

(b) $G/S = 0.40$

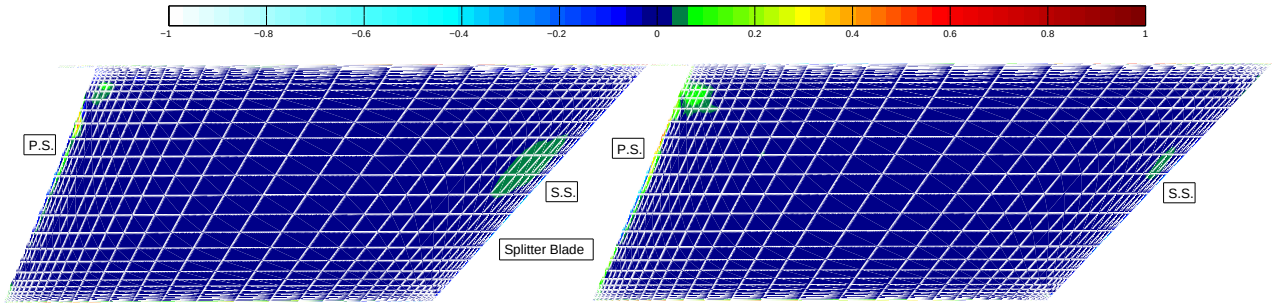

(c) $G/S = 0.60$

Figure 3-4: Difference of time and volume averaged entropy generation between each vaned case and the vaneless case at 99% impeller chord. Normalized by the time and volume averaged dissipation rate for the entire vaneless plane, $\frac{\overline{\rho \frac{Ds}{Dt}}^{\mathbf{t},\mathbf{V}}_{j,k} - \overline{\rho \frac{Ds}{Dt}}^{\mathbf{t},\mathbf{V}}_{VC_{j,k}}}{\overline{\rho \frac{Ds}{Dt}}^{\mathbf{t},\mathbf{V}}_{VC_{i=99\%}}}$

	Mean	Standard Deviation, σ	Maximum	Minimum
$G/S = 0.28$	-0.007	0.95	16.59	-13.25
$G/S = 0.40$	0.005	0.201	4.43	-3.18
$G/S = 0.60$	0.036	0.074	2.02	-1.01

Table 3.2: Summary of relative dissipation changes at the impeller trailing edge plane for all vaned geometries compared to the vaneless case

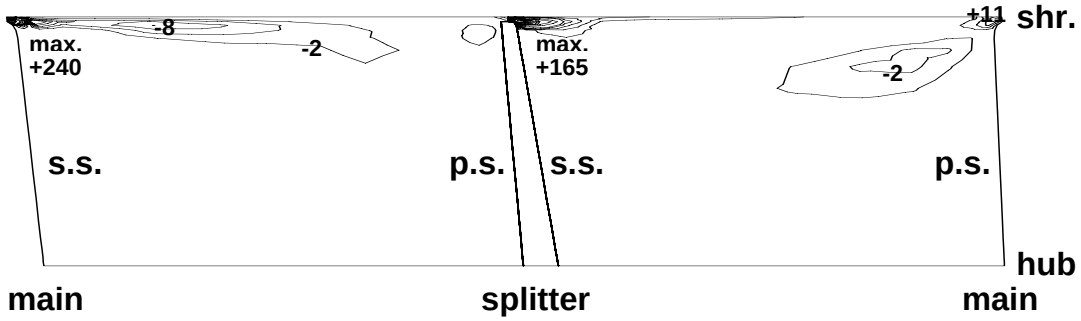

(a) $G/S = 0.30$

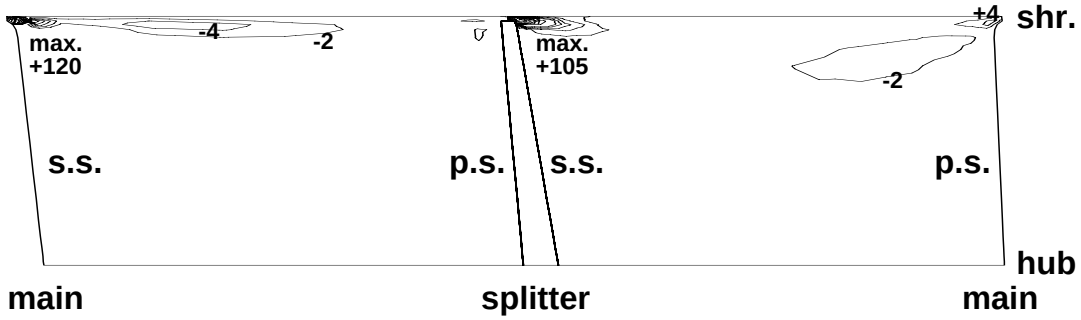

(b) $G/S = 0.50$

Figure 3-5: Difference of time and volume averaged entropy generation between Shum's two vaned cases and his vaneless case at 99% impeller chord. Normalized by the time and volume averaged dissipation rate for the entire vaneless plane, $\frac{\overline{\rho \frac{Ds}{Dt}}^{\mathbf{t},\mathbf{V}}_{j,k} - \overline{\rho \frac{Ds}{Dt}}^{\mathbf{t},\mathbf{V}}_{VC_{j,k}}}{\overline{\rho \frac{Ds}{Dt}}^{\mathbf{t},\mathbf{V}}_{VC_{i=99\%}}}$. From [3]

	$G/S = 0.28$	$G/S = 0.40$	$G/S = 0.60$	$Vaneless$
$\frac{\Delta A_{eff}}{A_{eff}}$	-0.0069	-0.0029	0.0017	
$\frac{T_{ITE}\,(s_{ITE}-s_{ILE})}{\frac{1}{2}U^2}$	0.0863	0.0859	0.0857	0.0857
$\frac{\Delta s_{ITE}}{c_p}$	2.06x10^{-4}	5.61x10^{-5}	7.88x10^{-7}	
θ	$-51.73°$	$-51.70°$	$-51.67°$	$-51.60°$
$\Delta\theta\ [radians]$	0.0023	0.0017	0.0012	

Table 3.3: Interaction related changes at the impeller exit for the independent variables of Shum's one-dimensional model

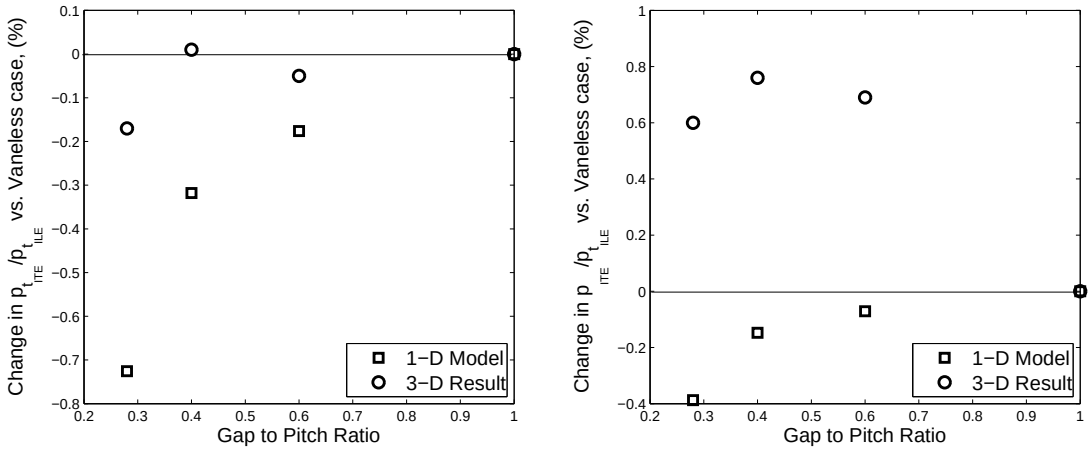

Figure 3-6: Stagnation and static pressure changes due to varying gap to pitch ratios shown with data from numerical simulation and Shum's one dimensional model

	$G/S = 0.28$	$G/S = 0.40$	$G/S = 0.60$
Loss	$-.12\%$	-0.03%	-0.00%
Blockage	-0.50%	-0.21%	-0.12%
Slip	-0.10%	-0.07%	-0.05%
Total	-0.73%	-0.32%	-0.18%

Table 3.4: Contribution of individual terms to total pressure changes in the one-dimensional model

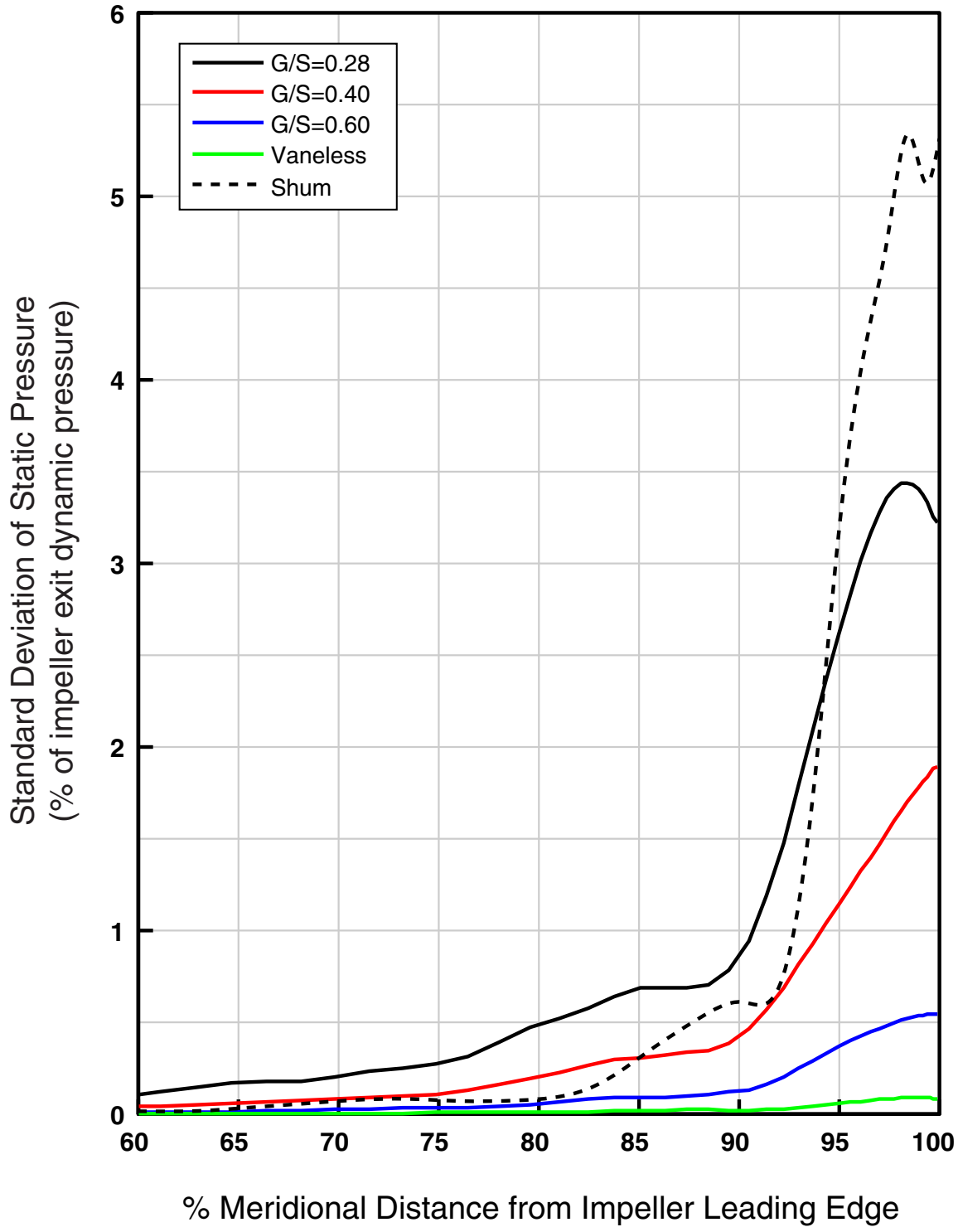

Figure 3-7: Comparison of mid-channel unsteadiness levels in the impeller, $\frac{\sigma(p)}{\frac{1}{2}\rho v_{ITE}^2}$

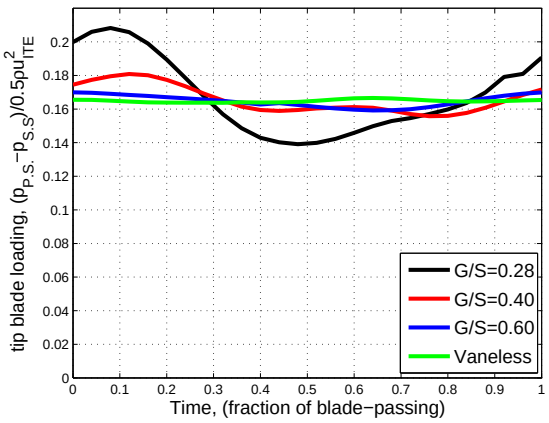

(a) 90% impeller chord

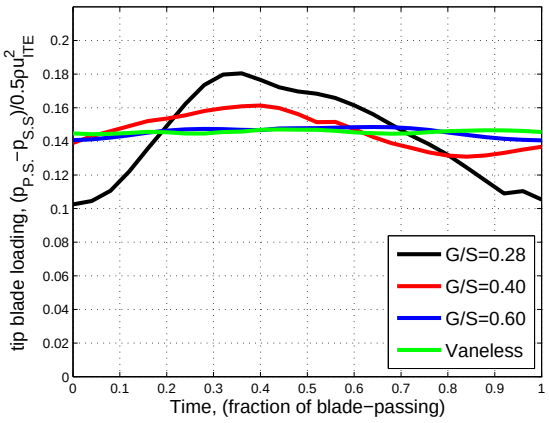

(b) 95% impeller chord

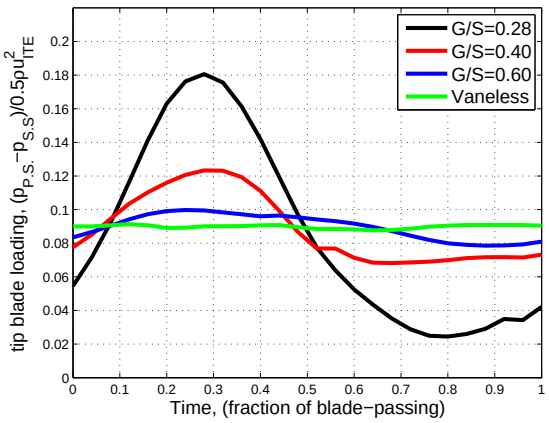

(c) 99% impeller chord

Figure 3-8: Comparison of loading over the blade-casing gap at three meridional impeller locations, $\frac{(p_{P.S.}-p_{S.S})}{\frac{1}{2}\rho v^2_{ITE}}$

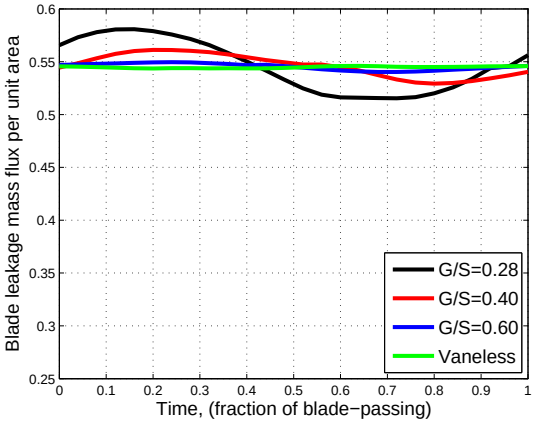

(a) 90% impeller chord

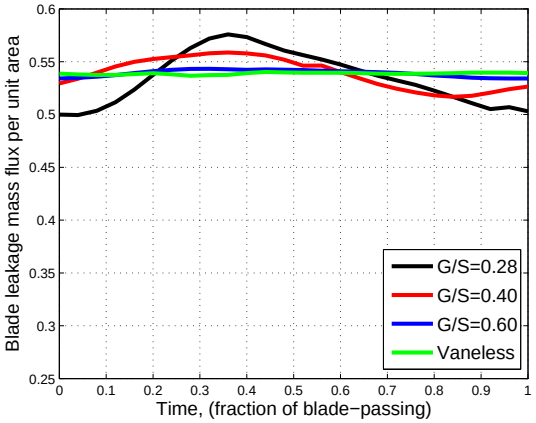

(b) 95% impeller chord

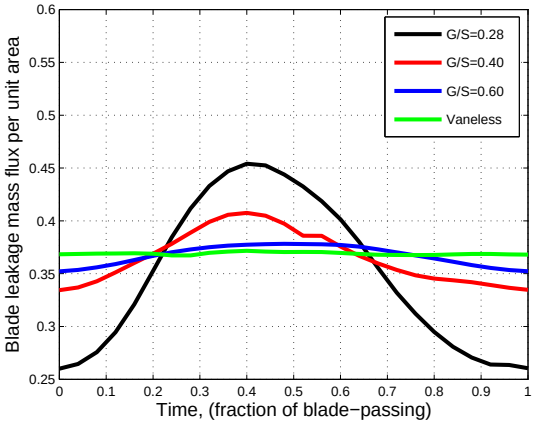

(c) 99% impeller chord

Figure 3-9: Comparison of blade leakage mass flux per unit area at three meridional impeller locations, $\frac{\rho w_{BCG}}{\rho v_{ITE}}$

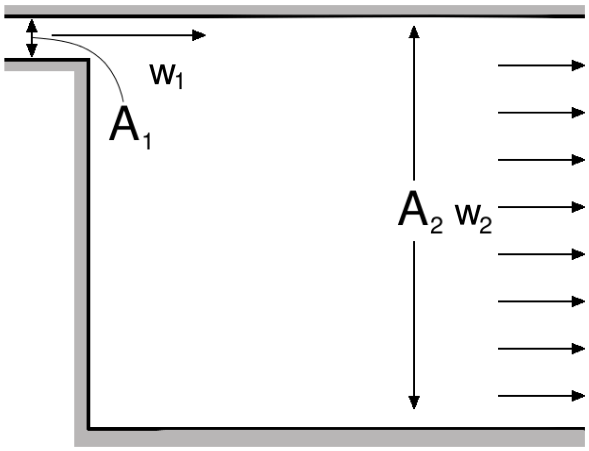

Figure 3-10: Schematic of one dimensional blade leakage model

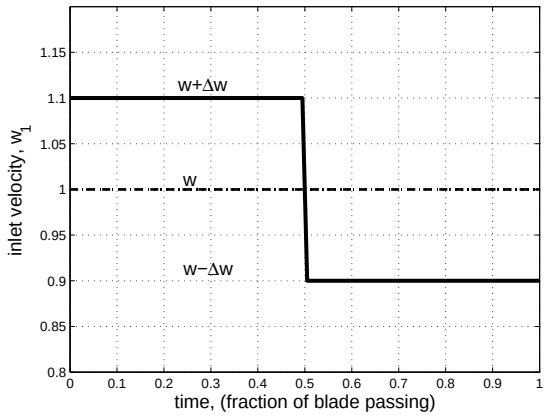

Figure 3-11: Example of square wave used in one dimensional jet total pressure loss model

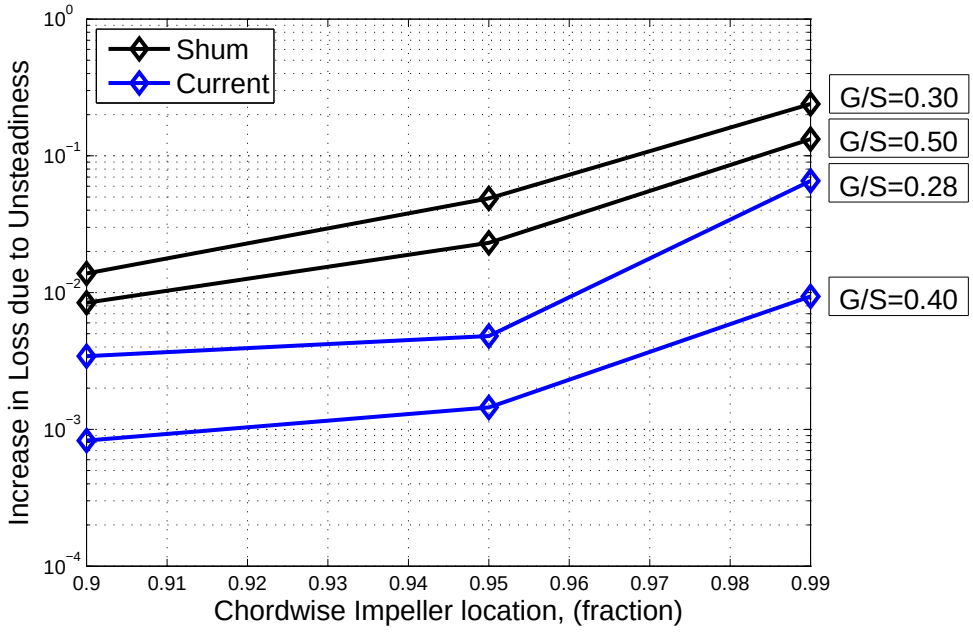

Figure 3-12: Estimated increase in time averaged, mixed out loss of blade leakage flow due to unsteadiness of the blade leakage jet, $\frac{T_t\left(\overline{\Delta s^t}-\Delta s_{steady}\right)}{\frac{1}{2}\overline{w_1}^2}$

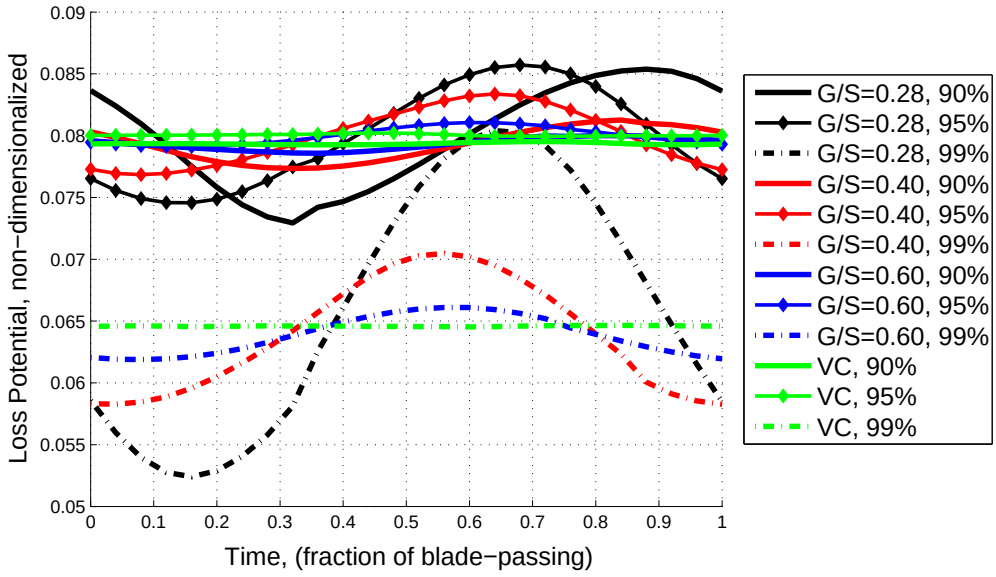

Figure 3-13: Comparison of loss potential, ξ, over one blade passing period between all G/S ratios and at three meridional locations within the impeller

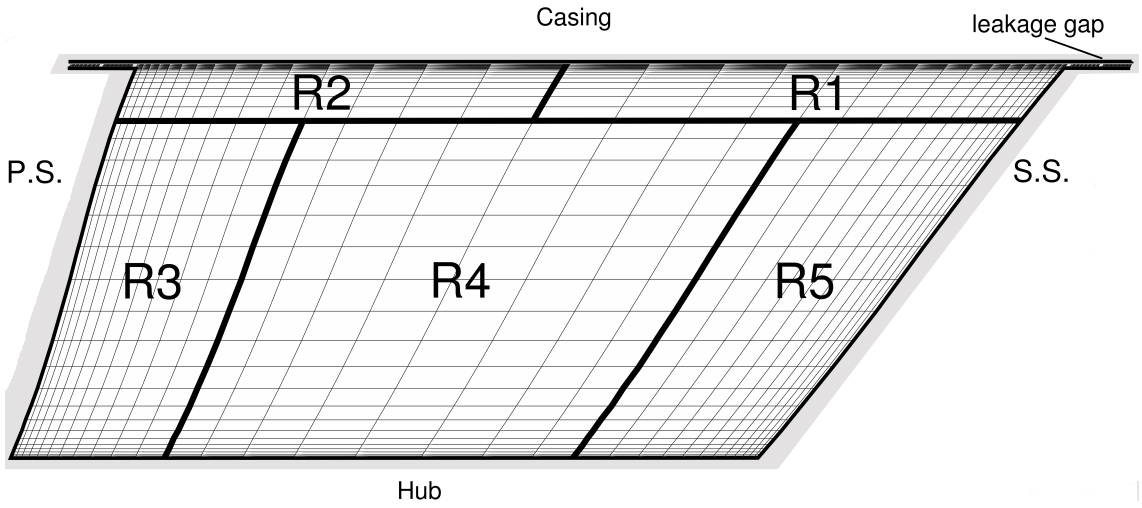

Figure 3-14: Schematic of regions used to conduct region-relative loss potential analysis. Cross section is a meridional plane of one impeller passage taken near the impeller trailing edge

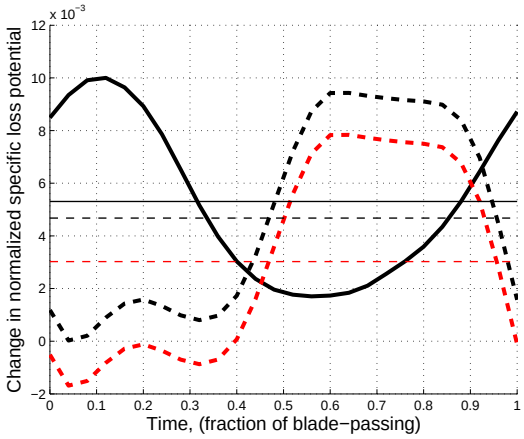

(a) $\delta i = 90\% - 91\%$ impeller chord

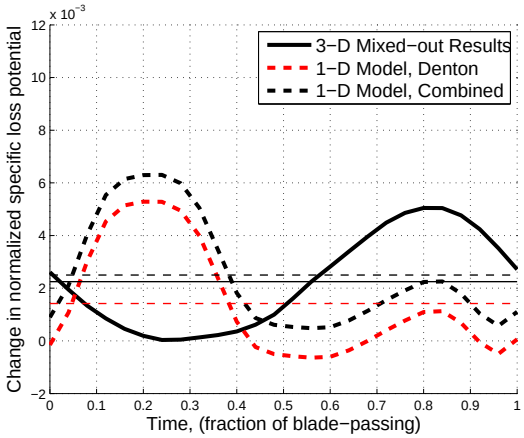

(b) $\delta i = 95\% - 95.5\%$ impeller chord

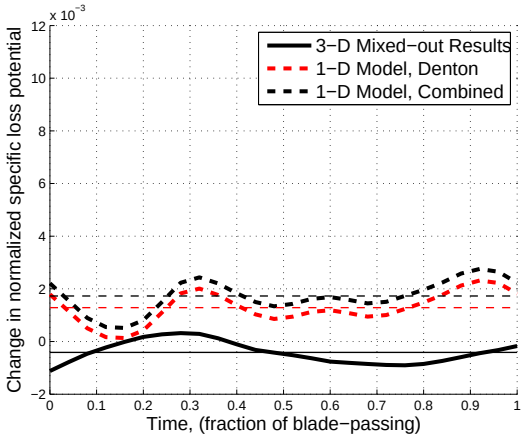

(c) $\delta i = 99\% - 99.5\%$ impeller chord

Figure 3-15: Change of $R1$ relative specific loss potential, $\Delta\xi$, over δi for $G/S = 0.28$ using three evaluation methods. Mean values shown as thin horizontal lines

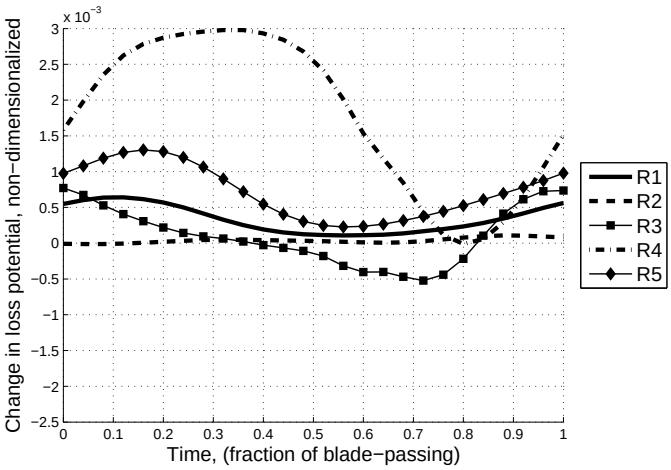

(a) $\delta i = 90\% - 91\%$ impeller chord

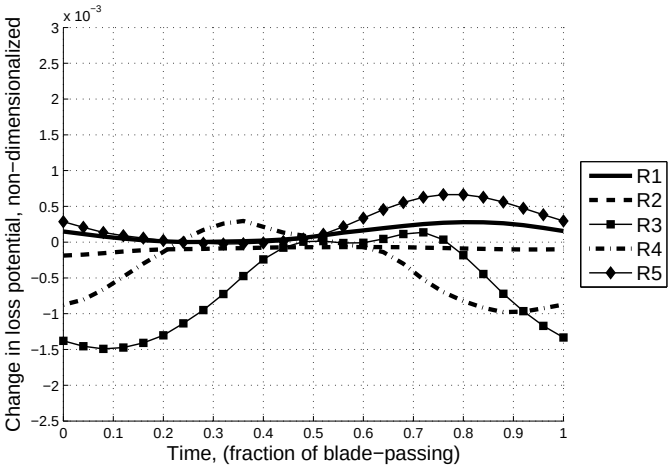

(b) $\delta i = 95\% - 95.5\%$ impeller chord

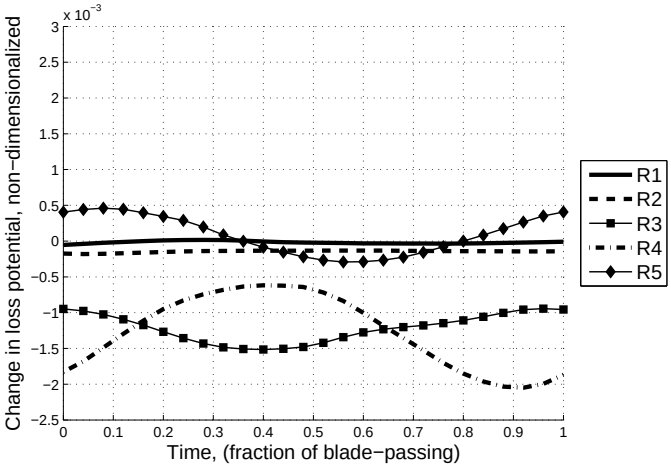

(c) $\delta i = 99\% - 99.5\%$ impeller chord

Figure 3-16: Change of passage relative specific loss potential, $\Delta\xi$, over δi for regions $R1$-$R5$ evaluated with numerical results from TURBO

Chapter 4

Summary and Conclusions

A set of numerical simulations has been conducted to assess the hypothesis that the gap to pitch ratio characterizes changes in impeller performance associated with unsteady impeller-diffuser interaction. The following sections summarize the findings of the investigation and offer suggestions as to where future work should be focused to continue making progress on developing a quantitative understanding of impeller-diffuser interaction.

4.1 Summary of Findings

4.1.1 Assessment of Hypothesis

It has been shown that the impeller performance response does not scale with the gap to pitch ratio as the hypothesis put forward by Murray suggests. In fact, no measurable performance change due to interaction was observed for the impeller of any vaned case relative to the vaneless case. For the conditions under which this computational experiment was conducted, this leads to the conclusion that:

- The hypothesis that the impeller performance change due to impeller-diffuser interaction can be described by a universal curve as a function of the gap to pitch ratio has been disproven

Murray's hypothesis was derived, in part, from consideration of the upstream propagation of a pressure disturbance originating at the diffuser leading edge. In formulating his hypothesis, he chose only to account for the decay rate (the gap to pitch ratio) and not the amplitude of the disturbance produced by the diffuser.

4.1.2 Key Findings

Two important observations have been made in this study which suggest that the amplitude of the pressure perturbation generated at the leading edge of the diffuser should be included as one of the parameters (in appropriate dimensionless form) for estimating performance change due to impeller-diffuser interaction. The first is that the impeller passage unsteadiness for the CC3 scales with gap to pitch ratio, only because the amplitude of the initial pressure perturbation produced by the diffuser was kept nearly constant. The second is that the unsteadiness level, which is much less than that of Shum's for the same gap to pitch ratio, fails to produce significant performance changes in the impeller. Together, these observations point to the need for parameters to quantify the level of unsteadiness as well as how this unsteadiness manifests itself as an actual change in performance. Both of these factors are lacking in Murray's hypothesis.

- Impeller unsteadiness level, as measured by the standard deviation of static pressures along the impeller passage centerline, is found to scale exponentially with the gap to pitch ratio only when the amplitude of the initial pressure perturbation produced by the diffuser remains constant

- Additions to the hypothesis are needed in order to relate the level of impeller passage unsteadiness to the level of performance change due to interaction. For example, the ratio of the unsteady amplitude, of blade leakage velocity or blade loading, to the time average value appears to be a parameter capable of quantifying the impact of unsteadiness on impeller performance change

4.2 Future Work

Considering the second point from section 4.1.2, above, in some detail, and with regards to some of the work done here, opens several possible areas of work for future research. First, we must consider three important pieces of information necessary to characterize the performance change that impeller-diffuser interaction has on the impeller: the initial magnitude of the pressure perturbation produced by the diffuser, the evolution of this perturbation as it travels upstream to the impeller, and the manner in which this perturbation manifests itself as performance change within the impeller. The disproven hypothesis of Murray only accounts for one of these factors.

Forming a hypothesis that includes these three items might be accomplished by considering the relative unsteadiness parameter written in terms of loading instead of velocity. Since Shum and Murray both concluded that change in the blade leakage flow is the primary mechanism by which interaction affects performance, it follows that the relative unsteadiness parameter, which describes the unsteady loss in the blade leakage flow, would be suitable for characterizing performance change due to interaction. Loss scales as the square of the relative unsteadiness parameter. Relating this to loading yields:

$$\left(\frac{w_{BCG_{MAX}} - w_{BCG_{MIN}}}{\overline{w}_{BCG}}\right)^2 \quad \propto \quad \frac{\left[(\Delta p)^{1/2}_{BCG_{MAX}} - (\Delta p)^{1/2}_{BCG_{MIN}}\right]^2}{\overline{(\Delta p)}_{BCG}} \tag{4.1}$$

The relative unsteadiness parameter can be addressed in terms of its two components:, the denominator, which quantifies the mean value of velocity or loading through the blade-casing gap, and the numerator, which quantifies the unsteady amplitude of velocity of loading through the blade-casing gap.

The inclusion of the mean blade loading term in describing interaction effects provides an estimate of how a given level of unsteadiness translates into a performance change for a certain compressor. If the mean loading is high, then changes in the impeller performance will be relatively less sensitive to a given unsteady loading amplitude than a compressor who has a low mean loading and is subjected to the

same unsteady amplitude. This is because it is the *ratio* of the unsteady amplitude to the mean value that characterizes a performance change. The same change in performance due to interaction would occur for a compressor (constant mean loading value) that is subjected to two different unsteady loading amplitudes, as is the case here with the CC3.

Figures 3-8 and 3-9 show that the mean loading values and mean mass flux values are independent of interaction level, and are therefore properties inherent to the impeller. Thus, the mean loading value may be found from CFD, or estimated using analytical methods such as those developed by Johnston, [25]. Since the merits of these methods have not been evaluated here, we will leave the determination of the most effective method to future studies and simply refer to the mean impeller blade loading as:

$$\frac{\overline{(p_{P.S.} - p_{S.S})}^{\mathbf{t}}}{\frac{1}{2}\overline{\rho}_{ITE}\overline{v}^2_{ITE}} \tag{4.2}$$

The numerator of the relative unsteadiness parameter represents the amplitude of the unsteady fluctuations in velocity and loading. Equation 4.1 reveals that the relative unsteadiness parameter in terms of velocity does not scale directly with that written in terms of loading. As well, the specific manner in which the amplitude of static pressure unsteadiness (quantified in figure 3-7) is related to the amplitude of unsteady loading across the impeller blades is not immediately clear. It is expected that with some additional work this numerator can be quantified in the manner suggested by equation 2.3, which accounts for the effects of the initial perturbation magnitude, $p'(0,0)$, and its exponential decay as described by the gap to pitch ratio.

Combining the numerator and denominator returns the form of the relative unsteadiness parameter, written in terms of loading, which has been shown to effectively describe the scaling of changes in performance loss due to interaction in the impeller. Therefore, the form of this parameter that may be shown to characterize impeller

performance change due to impeller-diffuser coupling looks like:

$$\Delta\pi \ , \ \Delta\eta \ \sim \ f\left(\frac{g\left(p'(0,0)e^{\left(\frac{-2\pi}{\sqrt{1-M_r^2}}\frac{G}{S_D}\right)}\right)}{\left(\overline{p_{P.S.}-p_{S.S.}}^{\mathbf{t}}\right)}\right) \tag{4.3}$$

Where $f()$ and $g()$ are two functions which have yet to be determined. For consistency between compressors, all terms are evaluated at the impeller trailing edge.

Characterizing performance change due to interaction in the manner of the relative unsteadiness parameter addresses the three criteria mentioned above: the disturbance evolution with gap to pitch ratio, as Murray's hypothesis does, plus two effects that Murray's hypothesis does not: the disturbance producing characteristic of the diffuser ($p'(0,0)$), and the sensitivity of the impeller to unsteadiness (mean loading)[1]. Recognizing this, the relative unsteadiness parameter, expressed in a form similar to that suggested in equation 4.3, has the potential to characterize the effect of impeller-diffuser interactions on impeller performance.

Depending on the magnitude of this parameter, any given compressor may find changes due to interaction to be more important in the impeller or more important in the diffuser. The current study saw low levels of the relative unsteadiness parameter, and relatively large performance changes in the diffuser (see Appendix D). Shum had high values of this parameter, and saw relatively large performance changes in his impeller. Therefore, changes in this parameter between different compressors may offer an explanation to the seemingly contradictory results obtained by Shum and Ziegler, [9].

The following recommendations are made for future work regarding impeller performance change due to impeller-diffuser interaction:

[1]It has been noted by some that highly loaded impellers are often more sensitive to unsteadiness than lightly loaded impellers. It is important to note that the sensitivity referred to here is in regards only to changes in the blade leakage flow, which Shum and Murray identified as the main mechanism of performance change due to interaction.

- Develop a model to estimate $p'(0,0)$ in various types of diffusers and at different operating points

- Determine the relationship between impeller passage unsteadiness, $p'(-G,0)$, and the impeller blade loading amplitude

- Evaluate the utility of the relative unsteadiness parameter in characterizing blade leakage loss due to unsteadiness for compressors in which the blade leakage flow is the dominant loss-producing mechanism due to impeller diffuser interaction

- Investigate the effect interaction on changes in diffuser performance

The last item on this list is of concern to the diffuser performance. Although Shum found these changes to be small relative to those of the impeller, it must be taken into consideration that this finding is true only at the operating point that Shum conducted his investigation. Over the range of operating mass flows between choke and stall, the incidence angle to the diffuser vanes changes significantly. As shown in, Appendix D, a change of incidence angle produces changes in diffuser performance. Because of this, the effect of interaction on diffuser performance is of significant engineering interest. In contrast to the data from Shum and Murray, the time averaged performance data here (for the impeller and the diffuser) is in alignment with the results of Ziegler, [9]. Although the sensitivity of the diffuser to interaction effects was not examined, we have seen that the impeller is not affected significantly. In this case, the diffuser performance may be of primary interest.

One possible mechanism of performance change in the diffuser due to impeller-diffuser interaction has been encountered and addressed in axial compressors by Botros, [15]. The loading and unloading of the impeller trailing edge over one blade passing period causes vortices of opposite sign to be shed periodically. The work of Botros suggests that entropy production depends on the shed vortex trajectory through the diffuser passage. This trajectory can be characterized by a ratio of two time scales: the time for vortex convection between blade rows, and the blade-passing

period. For a given operating mass flow and rotational speed, this ratio depends only on the radial gap length, which sets the convection time of the vortices between the impeller and diffuser. This effect may explain the disproportionate diffuser loss coefficients relative to incidence angle obtained here. It is suggested that this ratio of time scales should be investigated further as it pertains to interaction's influence on diffuser performance.

Appendix A

Acoustic Equation

The linear-theory equation for the propogation of a small disturbance in a medium is the acoustic equation, represented here with ϕ as the velocity potential.

$$\nabla^2\phi - \frac{1}{a_\infty^2}\frac{\partial^2\phi}{\partial t^2} = 0 \tag{A.1}$$

If we apply the Galilean transformation $x' = x + ut$, as suggested in [26], equation A.1 in two dimensions becomes

$$\frac{\partial^2\phi}{\partial x^2} + \frac{\partial^2\phi}{\partial y^2} - \frac{u^2}{a_\infty^2}\frac{\partial^2\phi}{\partial x^2} = 0 \quad \rightarrow \quad (1 - M_\infty^2)\frac{\partial^2\phi}{\partial x^2} + \frac{\partial^2\phi}{\partial y^2} = 0 \tag{A.2}$$

From here a coordinate transformation is made of the form $x^* = x/(1 - M_\infty^2)$ and $y^* = y$ after which equation A.2 becomes Laplace's equation.

$$\frac{\partial^2(\phi)}{\partial x^{*2}} + \frac{\partial^2(\phi)}{\partial y^{*2}} = 0 \tag{A.3}$$

The solution to Laplace's equation with the coordinate transformation can be found by following the form of equation 2.1. Next, M_∞ is replaced by the component of the Mach in the radial direction, the direction of the impeller, M_r. When evaluated with the characteristic length scales, as was done in equation 2.2, this yields an expression for the propagation of a pressure perturbation which accounts for the fluid velocity

in direction of the impeller.

$$p'(-G,0) = p'(0,0)e^{-\frac{2\pi}{\sqrt{1-M_r^2}}\frac{G}{S_D}} \tag{A.4}$$

Appendix B

Blockage

This appendix contains the details of how the quantification of relative blockage, equation 2.30, is developed. As was discussed earlier, the only component of velocity that contributes to blockage is the component in the mean flow direction. Therefore, only differences in the magnitude of velocity in the mean-flow direction can change the effective flow area between cases. In turbomachinery there is no convenient definition of the mean-flow direction, as there is in external aerodynamics, so we must define it. Our choice is to use the time and momentum-flux averaged velocity vector specific to a given chord-wise location , i, as calculated from the case of the vaneless-diffuser. Using the vaneless configuration provides a definition of mean-flow direction that is without the influence of interaction.

$$\hat{v}_{_{MFD}} = \frac{\vec{v}^{\mathbf{t,P}}}{\mid \vec{v}^{\mathbf{t,P}} \mid} \qquad \text{where:} \qquad \vec{v}^{\mathbf{t,P}}_{_{MFD}} = \frac{\int_i (\vec{v}) \vec{v} d\dot{m}}{\int_i \vec{v} d\dot{m}} \mid_{vaneless} \tag{B.1}$$

In two dimensions blockage can be simply calculated using the integral relation for the displacement thickness. For a case whose free-stream velocity is purely in the $+x$ direction this is:

$$\delta^* = \int_0^{y_{_E}} \left(1 - \frac{\rho \, v_x}{\rho_{_E} \, v_{_E}} \right) dy \tag{B.2}$$

δ^* can also be represented by a difference of mass flows:

$$\delta^* = \frac{\dot{m}_I - \dot{m}_V}{\rho_E v_E} \tag{B.3}$$

However, the derivation of the relations in B.2 and B.3 assume that the quantity $\rho_E\, v_E$ remains constant between the inviscid and viscous cases. For problems in internal flows it is often the mass flow that is held constant from case to case, not the quantity $\rho_E\, v_E$. Therefore, we must derive a new blockage expression which reflects the constraints of this experiment. Since we are interested in the relative change in blockage, and not its absolute value, we begin by writing an expression for $\Delta\delta^\star$, noting that both the mass flow and core quantity, $(\rho v)_{core}$, are case-specific.

$$\Delta\delta^\star = \left[\frac{\dot{m}_{inv} - \dot{m}_2}{(\rho_e\, v_e)_2}\right] - \left[\frac{\dot{m}_{inv} - \dot{m}_1}{(\rho_e\, v_e)_1}\right] \tag{B.4}$$

The inviscid mass flow, $\dot{m}_{inv}$ can be rewritten as $\dot{m}_{inv} = (\rho\, v)_{core}\, A$, where A is the geometric flow area. Simplifying equation B.4 and recognizing that the mass flow is the same for each case yields:

$$\Delta\delta^\star = \dot{m}\left(\frac{(\rho_e\, v_e)|_2 - (\rho_e\, v_e)|_1}{(\rho_e\, v_e)|_1 (\rho_e\, v_e)|_2}\right) \tag{B.5}$$

Intuitively, this equation makes sense: if case 2 has more blockage than case 1, a larger core quantity is required to pass the same mass flow. Equation B.5 will serve as the foundation for the analagous three dimensional relation.

Next we must properly define the core quantity, $(\rho v)_{core}$. To alleviate the difficulties that Khalid, [24], and Shum, [3], encountered in defining proper values for this quantity in unsteady, turbulent flows, it is desired to develop a method that removes user-defined dependencies entirely. To do this without arbitrariness and in a repeatable fashion, we seek a method that integrates over the entire channel cross section. The accuracy of this method is not expected to be high because we include even the very low velocity regions, but because we are measuring relative differences

in blockage these differences are tolerable as long as the precision is good. High precision from case to case will offset the systematic errors due to the integration itself. In formulating this integral quantity we identify the characteristics consistent with a core-flow and target them explicitly. They are:

- High mass flux, $\rho v A$
- High momentum flux, $\rho v^2 A$
- Low gradient of velocity, $\frac{\partial v}{\partial x_i}$
- Low Laplacian of velocity, $\frac{\partial^2 v}{\partial x^2}_i$

The last term is included, perhaps not so obviously, to handle regions where core flow unaffected by viscosity can still maintain a velocity gradient such as in the channel of a rotating impeller. Using combinations of these characteristics, four integrals were constructed to average the core quantity, $(\rho v)_{core}$.

1. Mass flux averaging, $(\rho v)^{\mathbf{M}}$
2. Momentum flux averaging, $(\rho v)^{\mathbf{P}}$
3. Gradient weighted momentum flux averaging, $(\rho v)^{\mathbf{P}\nabla}$
4. Gradient and Laplacian weighted momentum flux averaging, $(\rho v)^{\Upsilon}$

The weighting factors are simply defined as $(1 - |Q|/|Q_{max}|)$, where Q is any quantity. This normalization method is effective only when the difference between the maximum and minimum values is of the same order as the standard deviation, ensuring a reasonable distribution. All velocities used in calculating $(\rho v)_{core}$ will be the component of local velocity in the mean flow direction, $\vec{v}_{MFD} = \vec{v} \cdot \hat{v}_{MFD}$. In equation form, option four is:

$$\overline{\rho\, v}^{\Upsilon}_{core} = \frac{\int_A \rho\, \vec{v}^{\,2}_{MFD} \left(1 - \frac{|\nabla \vec{v}|}{|\nabla \vec{v}|_{max}}\right) \left(1 - \frac{|\nabla^2 \vec{v}|}{|\nabla^2 \vec{v}|_{max}}\right) d\dot{m}}{\int_A \vec{v}_{MFD} \left(1 - \frac{|\nabla \vec{v}|}{|\nabla \vec{v}|_{max}}\right) \left(1 - \frac{|\nabla^2 \vec{v}|}{|\nabla^2 \vec{v}|_{max}}\right) d\dot{m}} \tag{B.6}$$

To evaluate the effectiveness of each option a two dimensional channel-flow model was constructed using four boundary layer profiles and various boundary layer thicknesses, δ. In all cases the core velocity is known and adjusts to maintain a constant mass flow as the prescribed boundary layer is altered. Each integral method was then applied to estimate the core velocity as well as the displacement thickness, $\delta^\star$. The profiles used, seen in figure B-1, are 1.) pure shear flow, 2.) an approximation of a Blasius boundary layer, 3.) a linearly advancing sinusoid to represent highly non-uniform boundary layers (similar to tip-leakage flow), and 4.)a core velocity exceeded by a jet/boundary layer combination.

Figure B-2 summarizes the important results of this analysis, plotting the error in core velocity predictions versus the true blockage as a percentage of geometric channel area. The results for eight boundary layer thicknesses from each of the four profiles are shown. In terms of our criteria for an acceptable method, the gradient and Laplacian-weighted averaging method produces the best results. The absolute error is the least of all methods, and the consistency (precision) of the error as blockage increases is the greatest of all methods, even as the blocked area reaches thirty percent of the channel.

Next, these same methods are applied to a sample of velocity profiles taken from the actual CC3 flowfield. Since no 'true' value of the core exists, the assignment of a single value to characterize a passage flow is very difficult. To gauge this value effectively, and upon the suggestion of Greitzer, [27], six fluid dynamicists were asked to evaluate the core velocity in eleven different velocity profiles taken from a range of locations within the CC3 impeller. Four of these profiles are shown in figure B-3. Comparing the human-estimated values with those of the gradient and Laplacian-weighted averaging method yielded an average error of $\epsilon = 1.74\%$ and a standard deviation of $\sigma = 3.02\%$. This result is satisfactory enough to apply this method of estimating the core quantity to the purposes of blockage quantification in this research. We can now replace the quantity $(\rho v)_{_{core}}$ by the time and weighted momentum-averaged quantity, $\overline{\rho v}^{\mathbf{t},\Upsilon}_{_{MFD}}$.

Subtracting equation 2.28 from itself for two separate cases and rearranging we

see that the normalized change in effective area is equal to the negative change in non-dimensional blockage.

$$\frac{\Delta A_{eff}}{A_{actual}} = -\Delta B \tag{B.7}$$

Since the absolute effective area is unknown, we have non-dimensionalized by the geometric flow area of the channel. The non-dimensional blockage, $-\Delta B$, can be replaced by $\Delta\delta^\star/A_{actual}$. Replacing the expression for $\Delta\delta^\star$ using equations B.6 and B.5, we arrive at:

$$\frac{\Delta A_{eff}}{A_{actual}} = \frac{\dot{m}}{A_{actual}} \left(\frac{\overline{\rho\, v}^{\mathbf{t},\Upsilon}\big|_{caseX} - \overline{\rho\, v}^{\mathbf{t},\Upsilon}\big|_{ref}}{\overline{\rho\, v}^{\mathbf{t},\Upsilon}\big|_{caseX} \overline{\rho\, v}^{\mathbf{t},\Upsilon}\big|_{ref}} \right) \tag{B.8}$$

Thus, the change in blockage for any case, denoted '$caseX$', relative to a reference case, 'ref', is given by equation B.8.

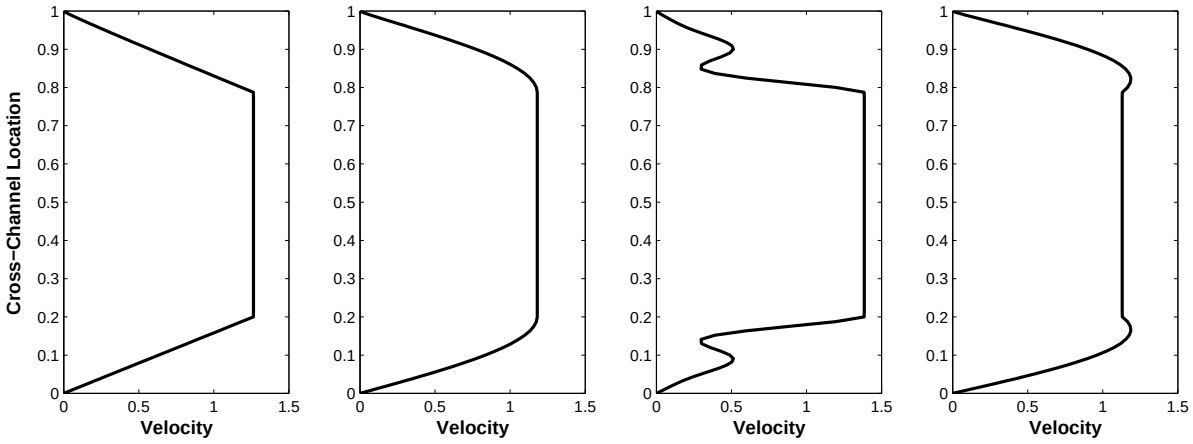

Figure B-1: Examples of two dimensional velocity profiles used to test core quantity averaging methods. Velocity is non-dimensionalized by the velocity that would pass an equivalent inviscid mass flow

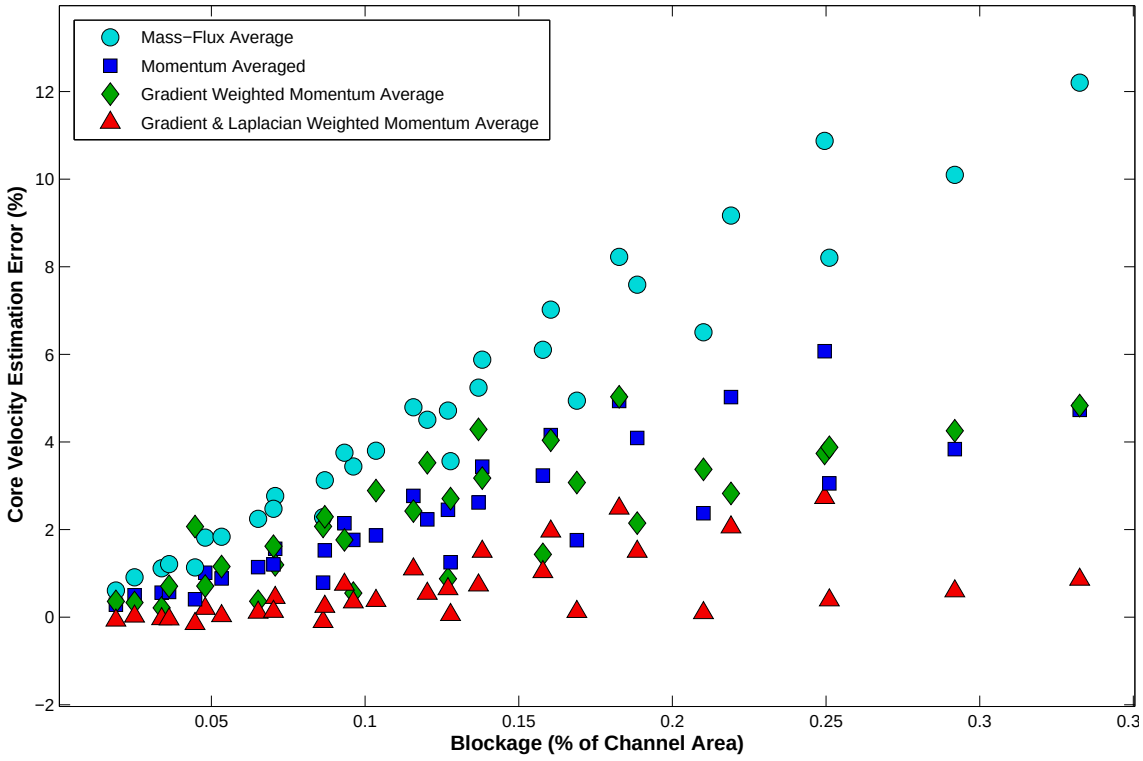

Figure B-2: Relative error of estimated core quantity, $(\rho v)_{core}$ versus fraction of channel blocked

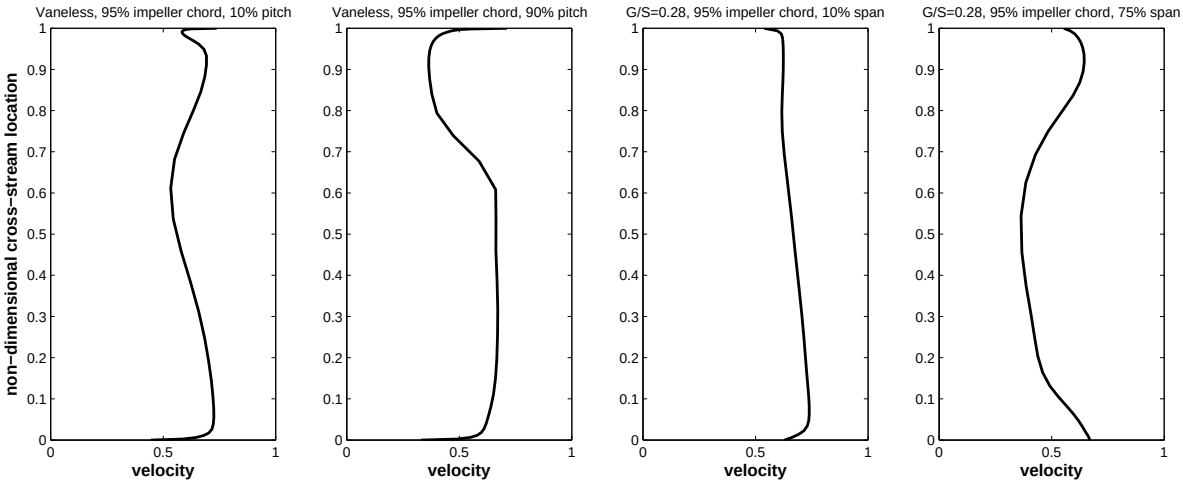

Figure B-3: Examples of two dimensional velocity profiles from CC3 flow fields used to test core quantity averaging methods, v_{MFD}/v_{ref}, where $v_{ref} = 287[m/s]$

Appendix C

Vane Positioning

This appendix contains the details of the swirl angle analysis highlighted in section 2.5.2. Beginning with equations C.1 and C.2 from Greitzer, et al [19], and assuming planar, isentropic, swirling flow.

$$\frac{dM^2}{M^2} = \frac{-2[1 + \frac{\gamma-1}{2}M^2]}{1 - M^2 cos^2\alpha}\frac{dr}{r} \tag{C.1}$$

$$d\alpha = \frac{[M^2 sin(2\alpha)]/2}{1 - M^2 cos^2\alpha}\frac{dr}{r} \tag{C.2}$$

All values in the above system of equations are known except that of $\alpha_{_{DLE}}$ and $M_{_{DLE}}$ (for any arbitrary value of the $r_{_{DLE}}$). Although we have two equations and two unknowns, the system is coupled and nonlinear. To simplify the solution process, it is assumed that an average value of the variable not being integrated for (i.e. α in the equation for dM^2/M^2) is sufficient to produce an accurate solution. An iterative code is written that offers an initial guess for $\alpha_{_{DLE}}$ and integrates equation 2.9, solving for $M_{_{DLE}}$. This value of $M_{_{DLE}}$ is then used to integrate and solve equation 2.10 for a new value of $\alpha_{_{DLE}}$, which is then substituted into equation C.1 and the cycle begins anew. This process is continued until the change in $\alpha_{_{DLE}}$ between iterations drops below a pre-specified tolerance.[1]

The new vane stagger angle is set by adding the true vane angle (Λ) to the change

[1]The accuracy of this method was verified against a numerical solver based on an explicit Runge-Kutta formula. Discrepancies between the two methods were less than 0.75% or 0.06°.

in swirl angle predicted by the model and the as-designed vane angle. In equation form:

$$\Lambda_{r,new} = \Lambda_{r,design} + (\alpha_{r,new} - \alpha_{r,design}) \tag{C.3}$$

When restaggering the vanes of the CC3, the vane itself is moved radially outward to the prescribed location, then rotated to align the chord of the vane with the associated stagger angle.

Appendix D

The Diffuser

This Appendix offers an explanation as to why the diffuser performance was not included in the main analysis. It was found that the incidence angle on the diffuser vane varied by more than $\Delta(\Lambda - \alpha_{_{DLE}}) = 4^\circ$ between cases. The tolerable range of time average incidence angles was estimated to be $\Delta(\Lambda - \alpha_{_{DLE}}) \leq 1^\circ$ by the data from Phillips, [1]. Above this tolerance the performance differences due to interaction could not be separated from performance differences due to the change in loading, boundary layer behavior, or area ratio stemming from incidence angle change. The pertinent performance summary of the diffuser of each case is given in table D.1, below.

Despite this variation of incidence angle, we can be certain that this variation of incidence angle had an influence on the behavior of the impeller that is secondary to the observed trends. This variation in diffuser vane incidence angle artificially increased the $p'(0,0)$ term for $G/S_{_D} = 0.40$ and even more so for $G/S_{_D} = 0.60$. The effect of this would be artificially high levels of interaction from these cases, relative to that of $G/S_{_D} = 0.28$. However, the standard deviation of pressures given in figure 3-7 shows unsteadiness levels well below that of the $G/S_{_D} = 0.28$ case. Because the unsteadiness levels for the two cases with artificially high incidence angles are not close in magnitude to that of our highest interaction case, and because they still scale with gap-to-pitch ratio, we conclude that the variation of incidence angle has only a minimal impact on the impeller's performance due to interaction. However,

	$G/S = 0.28$	$G/S = 0.40$	$G/S = 0.60$	$Vaneless$
Incidence angle, $\Lambda - \alpha_{_{DLE}}$	9.1°	10.2°	14.6°	N/A
Inlet Mach number, $M_{_{DLE}}$	0.817	0.793	0.754	N/A
Coefficient of Performance, C_{PR_D}	0.714	0.541	0.636	0.429
Coefficient of Loss, C_{loss_D}	0.136	0.188	0.142	0.154

Table D.1: Summary of diffuser performance

the impact of this variation on the diffuser performance is too large to separate any interaction related effects from those due to variation of incidence angle. Therefore, a meaningful investigation of the diffuser is unable to be pursued. However it should be noted that $G/S_{_D} = 0.40$ has the highest coefficient of loss, despite its incidence angle being only 1.1° larger than that of $G/S_{_D} = 0.28$. As mentioned in section 4.2, this may be of engineering interest and possibly approached using the $B3$ parameter as defined by [15].

The reason for the swirl angle deviations was not investigated. Future studies should carefully evaluate the assumptions regarding the impeller trailing edge flow when making swirl angle predictions.

Appendix E

Supplemental Figures

This appendix contains figures and data that supplement the material presented in the main text but was not needed to directly illustrate the ideas and draw meaningful conclusions. Each figure in this appendix is referenced specifically in the section it relates to.

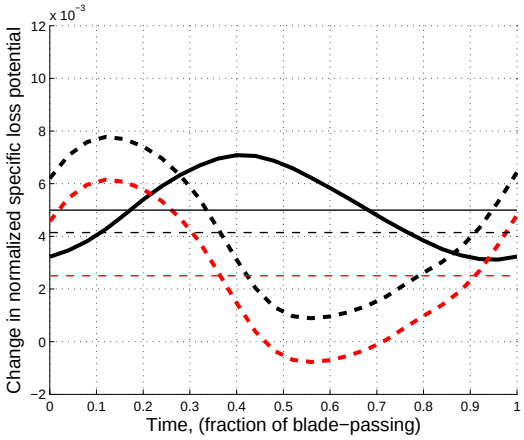

(a) $\delta i = 90\% - 91\%$ impeller chord

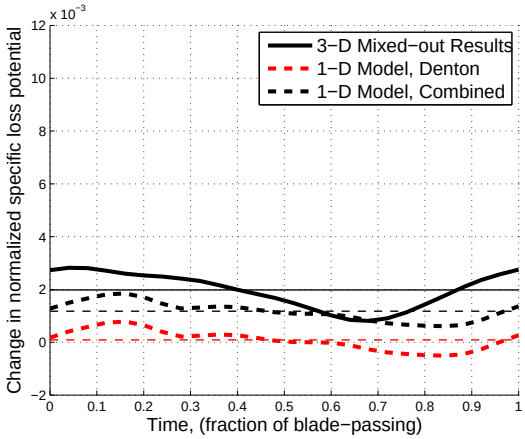

(b) $\delta i = 95\% - 95.5\%$ impeller chord

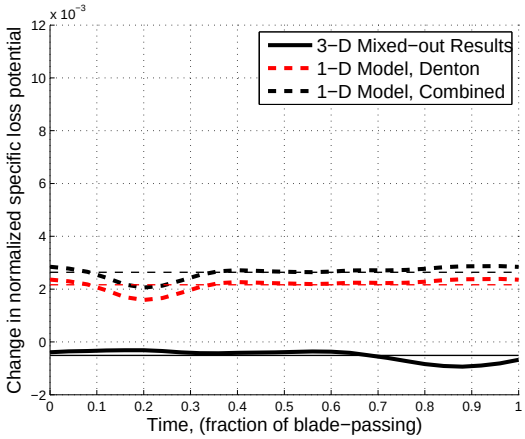

(c) $\delta i = 99\% - 99.5\%$ impeller chord

Figure E-1: Change of $R1$ relative specific loss potential, ξ, over δi for $G/S = 0.40$ using three evaluation methods. Mean values shown as thin horizontal lines

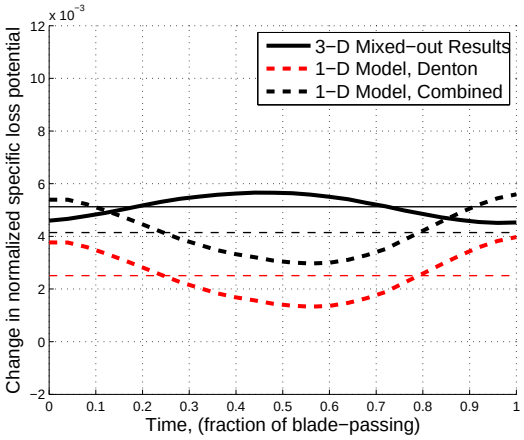

(a) $\delta i = 90\% - 91\%$ impeller chord

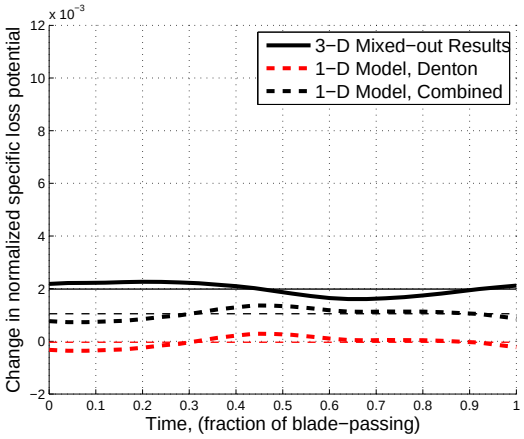

(b) $\delta i = 95\% - 95.5\%$ impeller chord

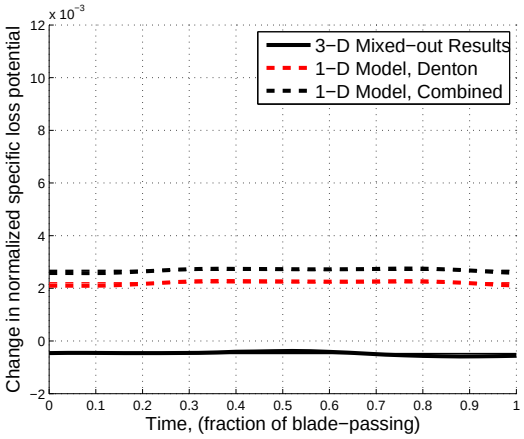

(c) $\delta i = 99\% - 99.5\%$ impeller chord

Figure E-2: Change of $R1$ relative specific loss potential, ξ, over δi for $G/S = 0.60$ using three evaluation methods. Mean values shown as thin horizontal lines

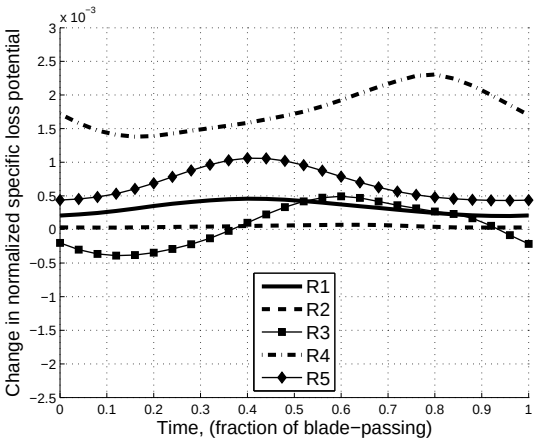

(a) $\delta i = 90\% - 91\%$ impeller chord

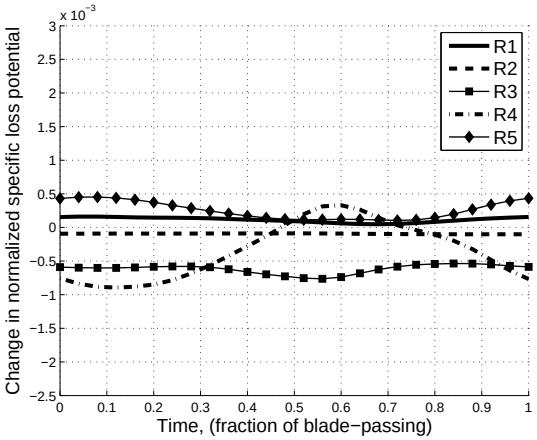

(b) $\delta i = 95\% - 95.5\%$ impeller chord

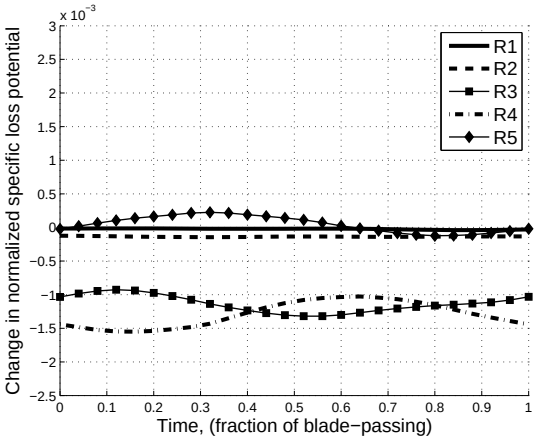

(c) $\delta i = 99\% - 99.5\%$ impeller chord

Figure E-3: Change of passage relative specific loss potential, ξ, over δi for regions $R1$-$R5$ evaluated with numerical results from TURBO

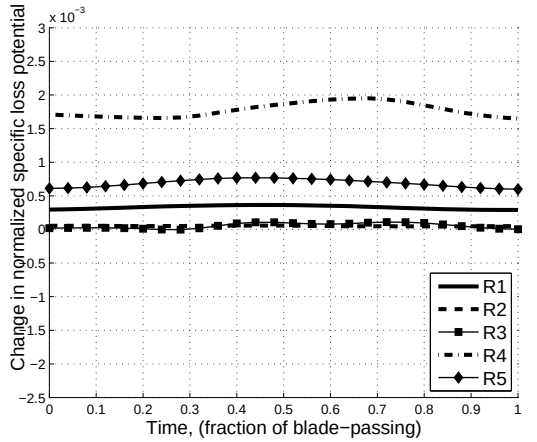

(a) $\delta i = 90\% - 91\%$ impeller chord

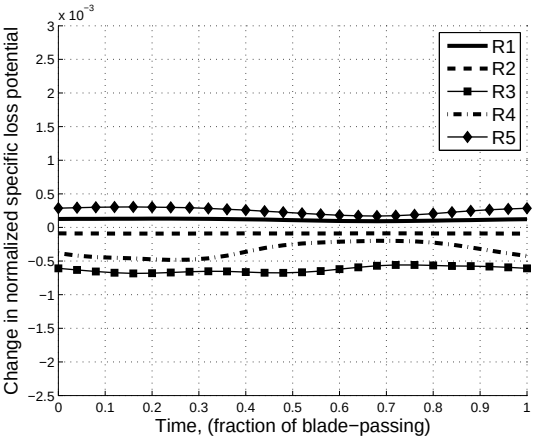

(b) $\delta i = 95\% - 95.5\%$ impeller chord

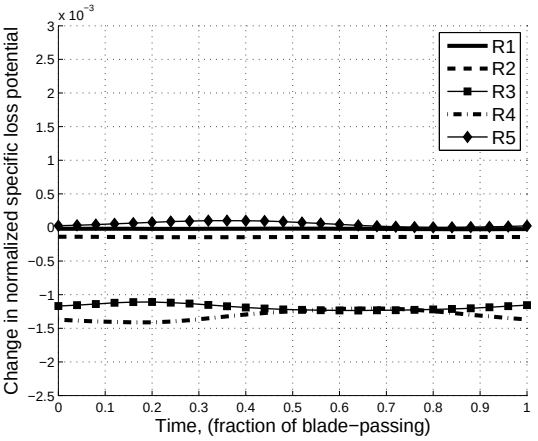

(c) $\delta i = 99\% - 99.5\%$ impeller chord

Figure E-4: Change of passage relative specific loss potential, ξ, over δi for regions $R1$-$R5$ evaluated with numerical results from TURBO

Bibliography

[1] M.S. Phillips. Role of flow alignment and inlet blockage on vaned diffuser performance. GTL Report 229, Massachusetts Institute of Technology, Gas Turbine Laboratory, Cambridge, MA, September 1997.

[2] G.J. Skoch and P.S. et al Prahst. Laser anemometer measurements of the flow field in a 4:1 pressure ratio centrifugal compressor. *Presented at Int'l Gas Turbine & Aeroengine Congress & Exhibition, Orlando, FL - June 1997*, 1997. ASME Paper 97-GT-342.

[3] Y.K.P. Shum. *Impeller-Diffuser Interaction in Centrifugal Compressors*. PhD dissertation, Massachusetts Institute of Technology, Gas Turbine Laboratory, February 2000.

[4] Mark Daly, editor. *Jane's Aero Engines*. Number 22. 2007.

[5] *The HF120*. http://www.gehonda.com/, 2006. Accessed 30 April, 2008.

[6] N.A. Cumpsty. *Compressor Aerodynamics*. Krieger Publishing Co., Malabar, FL, 2004.

[7] C. Rodgers. The performance of centrifugal compressor channel diffusers. *ASME Paper*, (82-GT-10), 1982.

[8] N.P. Murray. Effects of impeller-diffuser interaction on centrifugal compressor performance. Master's thesis, Massachusetts Institute of Technology, Gas Turbine Laboratory, February 2003.

[9] K.U. Ziegler, H.E. Gallus, and Reinhard Niehuis. A study on impeller-diffuser interaction - part i: Influence on the performance. *Journal of Turbomachinery*, 125:173–182, January 2003.

[10] K.U. Ziegler, H.E. Gallus, and Reinhard Niehuis. A study on impeller-diffuser interaction - part ii: Detailed flow analysis. *Journal of Turbomachinery*, 125:183–192, January 2003.

[11] T.F. McKain and G.J. Holbrook. Coordinates for a high performance 4:1 pressure ratio centrifugal compressor. *NASA Contractor Report*, 1997. No. 204134.

[12] Greg Herrick. *MSU TURBO Online Documentation*. Computational Simulation and Design Center at Mississippi State University, turbo p.v3 edition, January 2005.

[13] J.P. Chen and J. Barter. Comparison of time-accurate calculations for the unsteady interaction in turbomachinery stage. *AIAA Journal*, 1998. AIAA-98-3292.

[14] A.D. Villanueva. Characterization of the flow field response to vaneless space reduction in centrifugal compressors. Master's thesis, Massachusetts Institute of Technology, Gas Turbine Laboratory, May 2006.

[15] B.B. Botros. Impact of unsteady flow processes on the performance of a high speed axial flow compressor. Master's thesis, Massachusetts Institute of Technology, Gas Turbine Laboratory, February 2008.

[16] X. Wang and J.P. Chen. A post-processor to render turbomachinery flows using phase-lag simulations. *AIAA Journal*, (2004-615), January 2004. Presented at 42nd AIAA Aerospace Sciences Meeting and Exhibit, Reno, Nevada.

[17] C.J. Smythe. Forced response predictions in modern centrifugal compressor design. Master's thesis, Massachusetts Institute of Technology, Gas Turbine Laboratory, June 2005.

[18] M.D. Hathaway, J.P. Chen, and R. Webster. Time accurate unsteady simulation of the stall inception process in the compression system of a us army helicopter gas turbine engine. In *Proceedings of the 2003 User Group Conference*. IEEE Computer Society, September 2003.

[19] E.M. Greitzer, C.S. Tan, and M.B. Graf. *Internal Flow: Concepts and Applications*. Cambridge University Press, Cambridge, UK, 2004.

[20] V.G. Filipenco. Experimental investigation of flow distortion effects on the performance of radial discrete-passage diffusers. Technical Report 206, MIT Gas Turbine Laboratory, Sept 1991.

[21] S. Deniz. Effects of inlet flow field conditions on the performance of centrifugal compressor diffusers. Master's thesis, Massachusetts Institute of Technology, Department of Aeronautics and Astronautics, 1996.

[22] J.D. Denton. Loss mechanisms in turbomachines. *Journal of Turbomachinery*, 115:621–656, October 1993. The 1993 IGTI Scholar Lecture.

[23] N.A. Cumpsty and J.H. Horlock. Averaging non-uniform flow for a purpose. Number GT2005-68081, Reno-Tahoe, Nevada ,USA, June 2005. ASME Turbo Expo, Proceedings of GT2005.

[24] S.A. Khalid. *The Effects of Tip Clearance on Axial Compressor Pressure Rise*. PhD thesis, Massachusetts Institute of Technology, February 1995.

[25] J.P. Johnston. Radial flow turbomachinery. *Fluid Dynamics of Turbomachinery*, 1986. ASME Turbomachinery Institute.

[26] H.W. Liepmann and A. Roshko. *Elements of Gasdynamics*. Dover Publications, Inc., Mineola, NY, 2004.

[27] E.M. Greitzer. Personnel Communication, 2008.